STUDY OF THE SURFACE ROUGHNESS EVOLUTION IN FATIGUED 316L STAINLESS STEEL

by

YE WANG

Presented to the Faculty of the Graduate School of
The University of Texas at Arlington in Partial Fulfillment
of the Requirements
for the Degree of

MASTER OF SCIENCE IN MECHANICAL ENGINEERING

THE UNIVERSITY OF TEXAS AT ARLINGTON
May 2012

ACKNOWLEDGEMENTS

I am grateful to my thesis advisor Professor Haiying Huang for giving me the opportunity to be part of the Advanced Sensor Technology Laboratory. It was a wonderful research experience to work with her. Her patience and kindness, as well as her academic experience, have been invaluable to me.

I am extremely grateful to Dr. Efstathios I. Meletis for providing me to the access to the Veeco surface profiler, for the experimental part of the thesis. I would like to thank Dr. Wen S. Chan for serving on my thesis committee. I would like to express my gratitude to Mr. Kermit Beird, the machine shop supervisor, for his help and assistance during the fatigue specimen design and production.

I am highly indebted to my parents and my beloved fiancée for their unending encouragement and constant support throughout my career.

Finally, I would like to thank my former and current lab member Irshad Mohammad, Manjunath Shenoy, Deniz Incel, Srikar Deshmukh and Xiang Xu for all the help and serious academic discussions we have had which will be a large fortune for the rest of my life.

April 20, 2012

ABSTRACT

STUDY OF THE SURFACE ROUGHNESS EVOLUTION IN FATIGUED 316L STAINLESS STEEL

Ye Wang, M.S

The University of Texas at Arlington, 2012

Supervising Professor: Haiying Huang

Fatigue is a critical design consideration in many aerospace structures. As improvements are sought in overall performance, maintenance requirements, and total service life of modern aircrafts, the demands for fatigue control techniques, such as material design for fatigue resistance, reliable fatigue life prediction, and continuous material damage monitoring, have increased. The most common practices to ensure fatigue safety include: fracture mechanics based fatigue life prediction, periodic non-destructive inspections, and material processing control. Reasonable successes have been achieved by applying these three techniques to ensure the safe operation of aerospace structures. It is worth mentioning that most of the present fatigue control techniques are only applicable when there is a dominant crack in the service components, i.e. the crack propagation stage, while the fatigue initiation stage (the evolution of pronounced surface relief, such as Persistent Slip Bands (PSBs) formation, crack nucleation and micro-crack propagation etc), could constitute 90% of the fatigue life for some components. Developing a quantitative understanding of crack initiation processes, therefore, should be considered as one of the most important tasks in fatigue study. Because crack initiation is strongly controlled by the local micro-structural features, systematic study of crack initiation could reveal fundamental information about the underlying mechanisms of fatigue damages which in turn can be incorporated into life prediction modeling to evaluate future damage development. One major challenge of fatigue study during crack initiation is that no physical measurement has been identified to characterize material damage since it is dominated by randomly distributed plastic deformation and micro-crack clusters.

In this thesis, we study the feasibility of exploiting the plastic deformation-induced surface roughness as a diagnosis tool to assess the material damage at early fatigue life. Scanning Whitelight Interferometric Microscope (SWLI) was applied to quantitatively study the surface roughness evolution of polycrystalline 316L stainless steel fatigue specimen. We demonstrated that the surface roughness increased with fatigue cycles during the entire fatigue process. In addition, we discovered that surface roughness increases at early fatigue stage were contributed by slip band formation while surface roughness increases at later-stage fatigue were due to the out-of-plane displacement of adjacent grains. Crack initiation and development has also been identified.

TABLE OF CONTENTS

LIST OF ILLUSTRATIONS

Figure Page

LIST OF TABLES

Table Page

CHAPTER 1

INTRODUCTION

1.1 Definition of Material Fatigue

In materials science, fatigue damage is defined as the progressive and localized structural damage that occurs when a material is subjected to cyclic loading. During fatigue, the nominal maximum stress values are less than the ultimate tensile stress limit, and may be below the yield stress limit of the material.

Fatigue can be divided into several stages, including crack initiation, micro-crack nucleation, macro-crack growth, and final fracture. Damage characteristics associated with different fatigue stages are illustrated in Figure 1.1.

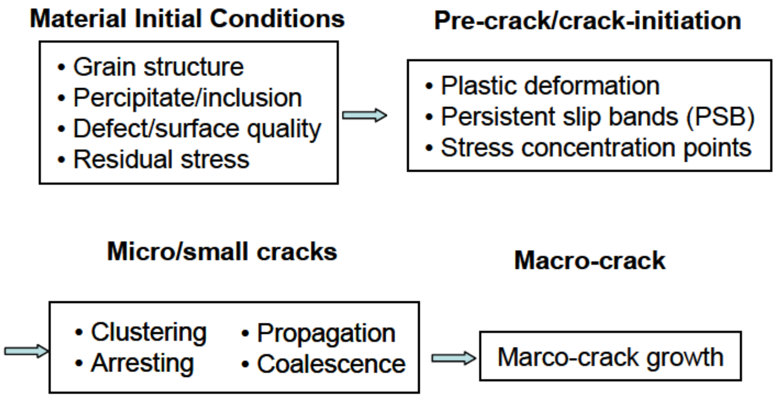

Figure 1.1: Material damage characteristics at different fatigue stages

1.2 Practices to Ensure Fatigue Safety

Fatigue is a critical design consideration in many aerospace structures. As improvements are sought in overall performance, maintenance requirements, and total service life of modern aircrafts, the demands for fatigue control techniques, such as material design for fatigue resistance, reliable fatigue life prediction, and periodic non-destructive inspections, have increased. All these techniques require the scientific understanding of fatigue processes. The study of fatigue problem has been approached from different disciplines in the past several decades. The most common practices to ensure fatigue safety include:

1.2.1 Fracture Mechanics Based Fatigue Life Prediction

The fracture mechanics approach to fatigue design assumes that all engineering components are inherently flawed. Based on this assumption, the useful life of a service component is defined as the time to propagate a dominant crack from its initial size to a critical dimension. A global fracture mechanics parameter, Stress Intensity Factor (SIF), is introduced to predict the growth rate of the crack, which in turn is employed to predict the remaining useful life of the structure. In general, the relationship between the SIF variation and the crack growth rate, i.e. Paris's law, is empirically obtained by fitting experimental data from laboratory tests of the specimens. A safety factor must be applied to compensate for uncertainties in the experimental data. Periodic inspections are also mandated to ensure that the service component is operating under designed conditions.

1.2.2. Structural Health Monitoring

Because of the empirical and global nature of the fracture mechanics based fatigue life prediction, it cannot account for micro-structural details, variations in material properties, and unexpected changes in environmental conditions. In order to deal with these insufficiencies, structural health monitoring techniques were developed to query the integrity of the service components, providing real-time assessment of their damage state. Structural health monitoring systems provide many advantages such as assessment of the material physical state on a continuous basis, potential elimination of catastrophic failures in operation, and reduction of down times and maintenance costs. However, most existing structural health monitoring systems can only detect cracks that are larger than a certain size and therefore are categorized as a “pass or fail” diagnostic system that warns only when the structure is no longer reliable.

1.2.3. Material Processing Control

Material processing control includes a series of operations that transforms industrial materials from a raw-material state into finished parts or products. For example, thermal treatment, including heat-treating and cold-treating, is a typical material processing control technology by which the temperature of the material is raised or lowered to alter the properties of the original material. Thermal treatment can help to release residual stress in material accumulated during cold work and reshape the material to gain better resistance to fatigue. Finishing process is another material processing control technology which can be employed to modify the surfaces of materials in order to protect the material against deterioration by corrosion, oxidation or deformation which will lead to early fatigue failure.

1.3 Limitation of the Present Practice to Predict Fatigue

Reasonable successes have been achieved by applying these three techniques to ensure the safe operation of mechanical structures, even though the basic mechanisms of fatigue were not understood fully. It is worth mentioning that most of the present fatigue control techniques are focused on the period when there is a dominant crack in the service components, i.e. the crack propagation stage. During the fatigue initiation stage (the evolution of pronounced surface relief, such as Persistent Slip Bands (PSBs) formation, crack nucleation and micro-crack propagation), which could constitute 90% of the fatigue life for some components, life prediction based on fracture mechanics may give non-conservative values [1]. Furthermore, exiting damage health monitoring systems are not sensitive enough to detect small changes in the material physical state. Developing a quantitative understanding of crack initiation processes, however, should be considered as one of the most important tasks in fatigue study. Because crack initiation is strongly controlled by the local micro-structural features, systematic study of crack initiation could reveal fundamental information about the underlying mechanisms of fatigue damage, which in turn can be incorporated into the life prediction model to evaluate future damage development. Investigation of crack initiation, however, is very challenging, due to the following considerations:

1. Material damage is dominated by plastic deformation-induced slip bands prior to crack nucleation. These slip bands are usually confined within individual grains and therefore are anisotropic in nature.

2. Once nucleated at the slip bands, micro-cracks generally have a length scale that is comparable to the characteristic micro-structural dimension of the material. Various micro-structural features such as grain boundaries, crystallographic orientation, grain mismatch, and phase difference could have a strong influence on their growth behavior.

3. Micro-cracks tend to cluster at certain region of the material instead of being uniformly distributed.

4. Micro-cracks display a bi-modal growth pattern; some micro-cracks can be retarded by a grain boundary or a brittle inclusion while the others will grow and coalesce with other micro-cracks, eventually becoming a dominated large crack that ultimately determines the final fracture of the service components.

These complicated characteristics of crack initiation cannot be quantitatively modeled by fracture mechanics, in which a single global physical measurement is employed to uniquely describe the crack behavior. In order to quantitatively characterize material damage at crack initiation stage, a physical measurement reflecting the intricate features of the micro-crack behavior is required.

1.4 History of Early Fatigue Study

The shape of the PSBs and the kinetics of their evolution have been the subject of numerous investigations since the beginning of the last century when only optical microscopes with limited resolution were available. As early as 100 years ago, Ewing and Humfrey used optical microscope to obtain micrographs of cyclic damage on specimen surfaces [2]. They found that the slip lines, later called PSBs, were developed in many grains of the polycrystalline materials, resulting in extrusions and intrusions on the polished surface. The first documented report of slip-induced surface roughening during fatigue was published by Forsyth [3].

The invention of the SEM provides more insight into the surface relief of PSMs and early damage evolution in fatigue because of its high resolution compared to ordinary optical microscope. With SEM, considerable progresses have been made in developing a detailed understanding of micro-structural changes induced by cyclic loading [4-8]. It was found that the most common cause of fatigue crack initiation in metals lies in the development of a damaging surface topography [9-12]. However, SEM can only provide 2D images of the sample surfaces but cannot provide quantitative depth information of the surface topography. Lacking a quantitative means to characterize this complex surface roughening phenomenon, the researchers used simple descriptive terms, such as surface roughness, peaks and notches, protrusions, intrusions, and extrusions, to generalize the surface topographic changes.

The invention of Atomic Force Microscope (AFM) in the early 1990s enabled the quantitative study of surface features in strained and cyclically strained materials. By scanning a sharp stylus over a surface, an AFM is capable of imaging solid samples with a sub-micron lateral resolution and a sub-Angstrom scale vertical resolution [13]. Harvey et al. was among the first to utilize AFM to obtain quantitative information on slip spacing and slip height displacements in cyclically loaded polycrystalline titanium and high strength-low alloy steel [14]. PSBs consist of not only local elevations, known as surface extrusions but also local depressions, known as surface intrusions. Usually, only the true extrusion height can be obtained in direct AFM measurement. Intrusions were first revealed by AFM using plastic replicas by Nakai et al in 1999 [15]. The association of AFM with electron back scattered diffraction (EBSD) was shown to represent a very useful combination for obtaining topographic and crystallographic aspects of fatigue damage [16]. Recently, several researchers [16-18] employed AFM to perform quantitative measurements of the slip bands and to study the evolution of surface topological features at different fatigue stages. Their preliminary results indicated that the surface roughness clearly increases as fatigue cycles increase. However, because of the limited scanning range of the AFM, it was found that the measured surface roughness is strongly affected by the scan location, leading to large scatter.

1.5 Plastic Deformation-induced Surface Roughness

One major challenge of early fatigue study is that no physical measurement has been identified to characterize material damage when it is dominated by highly localized plastic deformation and micro-crack clusters. To facilitate fatigue study at early fatigue life, we propose to use the plastic deformation-induced surface roughness as a diagnosis tool to assess the material damage before large cracks emerge. It has been long known to the material scientists that all fatigue cracks start with plastic deformation [2-3], [19-20]. Plastic deformation, in turn, will cause the roughening of the specimen surface. Surface roughness changes, therefore, are directly related to the plastic deformations experienced by the specimen.

Compared to existing fatigue study methodologies, the proposed methodology possesses the following advantages:

1) Enable early damage detection: Before crack nucleates, material damage is manifested through plastic deformation induced surface roughness. Therefore, monitoring the specimen surface changes can identify a potential crack initiation spot even before a micro-crack emerges. In addition, plastic deformation around a micro-crack is usually much larger than the micro-crack itself. As such, material damage detection based on surface roughness monitoring can be much more sensitive than techniques detecting the micro-crack directly.

2) Facilitate investigation of micro-structural influences: it is well known that material fatigue life is strongly influenced by the microstructures such as grain size, grain orientation, precipitation, and inclusions. Since the same mechanisms also govern the plastic deformation development, systematic study of the surface roughness changes could help identifying the intrinsic microstructure features that govern the material fatigue life.

3) Full field measurement: Instead of having a dominant large crack, material damage at early fatigue life takes the form of plastic deformations and micro-crack clusters, whose highly localized, heterogeneous, and anisotropic nature cannot be characterized by a single global variable such as crack length or stress intensity factor. A full-field surface topographic image reveals the plastic deformation experienced by the material and therefore is ideal for capturing this complex phenomenon in detail.

4) Non-destructive: Because material damage development is progressive, a non-destructive measurement technique is desired to track the evolution of the surface roughness. Combined with a CCD camera, the optical surface profiler can perform non-contact 3D surface profiling of the specimen without disturbing the specimen or the experimental set-up.

1.6 Thesis Overview

In this thesis, surface roughness evolution in fatigues 316L stainless steel was quantitatively studied by SWLI. Chapter 2 provides the background information about surface roughness and its measurement. Chapter 3 describes the fatigue specimen design, fatigue experiment setup and SWLI setup. Chapter 4 discusses the surface roughness measurement results in details and explains the mechanism for the surface roughness increase. Chapter 5 focuses on the improvements of fatigue specimen design and fatigue experiment set up, presents its results and seeks the possible mechanism. Chapter 6 summarizes the conclusions and presents the future work.

CHAPTER 2

SURFACE ROUGHNESS AND ITS MEASUREMENT

2.1 Surface Roughness

2.1.1. Definition

Surface roughness is a measure of the texture of a surface. It is quantified by the vertical deviations of a real surface from its ideal form. If these deviations are large, the surface is rough; if they are small, the surface is smooth.

There are many different roughness parameters in use, but R_a is by far the most common. Other common parameters include R_q, R_z and R_t. Figure 2.1 is a surface profile which helps to illustrate the definition of these surface roughness parameter.

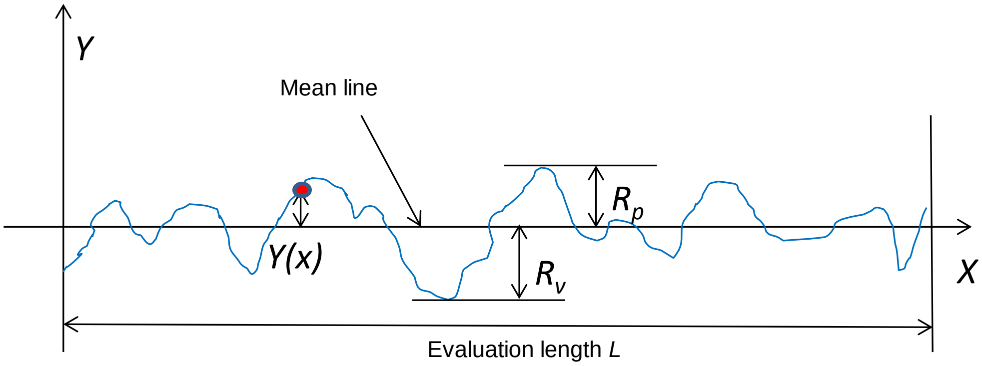

Figure 2.1: Surface profile along a single line

R_a is the arithmetic average roughness. It was defined as follows:

$$R_a = \frac{1}{L}\int_0^L |y(x)|dx$$

where, *L* is the evaluation length, *y(x)* is the height, *x* is the distance along measurement.

Similar to R_a, R_q represents the root mean squared roughness. It was defined as:

$$R_q = \sqrt{\frac{1}{L}\int_0^L y^2(x)dx}$$

L, y and x are the same as described in R_a.

R_t stands for maximum height of the profile. It was defined as:

$$R_t = R_p - R_v$$

where R_p is the maximum peak height and R_v is the maximum valley depth as shown in Figure 2.1.

R_z represents average height between the highest peak and lowest valley in each sampling length. Its definition is:

$$R_z = \frac{1}{s}\sum_{i=1}^{s} R_{ti}$$

where *s* is the number of sampling lengths, and R_{ti} is R_t for the i^{th} sampling length.

In the thesis, we choose the most common used R_a to be the measured surface roughness parameter.

2.1.2. Surface Roughness Measurement Techniques

2.1.2.1 Stylus Instruments

The first technique is stylus instruments which based on the principle of running a probe across a surface in order to detect variations in height as a function of distance [21]. AFM is one of stylus instruments. AFM uses a cantilever probe tip to detect weak forces on a specimen. While the sample moves in the x-y direction the pointed end of the cantilevered probe can either make contact with the specimen surface or function in a non-contact mode.

In the contact mode, the static tip deflection is used as a feedback signal. Because the measurement of a static signal is prone to noise and drift, low stiffness cantilevers are used to boost the deflection signal. However, close to the surface of the sample, attractive forces can be quite strong, causing the tip to "snap-in" to the surface. Thus static mode AFM is almost always done in contact where the overall force is repulsive. Consequently, this technique is typically called "contact mode". In contact mode, the force between the tip and the surface is kept constant during scanning by maintaining a constant deflection.

In non-contact mode, the tip of the cantilever does not contact the sample surface. The cantilever is instead oscillated at a frequency slightly above its resonant frequency where the amplitude of oscillation is typically a few nanometers (<10 nm). The van der Waals forces, which are strongest from 1 nm to 10 nm above the surface, or any other long range force which extends above the surface acts to decrease the resonance frequency of the cantilever. This decrease in resonant frequency combined with the feedback loop system maintains a constant oscillation amplitude or frequency by adjusting the average tip-to-sample distance. Measuring the tip-to-sample distance at each (x,y) data point allows the scanning software to construct a topographic image of the sample surface.

In these two modes, all of data can be collected by using lasers, piezoelectric sensors and photoelectric sensors as shown in Figure 2.2. A Laser is sent to the tip of AFM cantilever, and the photoelectric sensor is able to measure movement based on changes in the incident angle of laser caused by changes of cantilevers movement. The piezoelectric sensors send a voltage to a transducer whenever a movement from the cantilever is made. Figure 2.3 is the enlarged view of the cantilever beam. We can clear see the laser being transmitted down to the cantilever tip and how it is then transmitted up to the photodiode that will detect the incident angle [22]. This form of detection will allow for very small changes in the incident angle.

Errors can be introduced to roughness measurements when a stylus instrument is used because of several factors. Some of these factors are the size of the stylus, stylus load, stylus speed, and lateral deflection by asperities.

The effect of stylus size is illustrated in Figure 2.4, which is a schematic comparison of an actual profile against the traced profile. This effect becomes more significant as the curvature of the peaks and valleys decreases, or the magnitude of the slope increases [21]. Regarding the effect of stylus load, it has been found that plastic deformation can be induced on the surface of the measured specimen if a load much higher than the recommended by the standards is used, resulting variation in the measurement results [21].

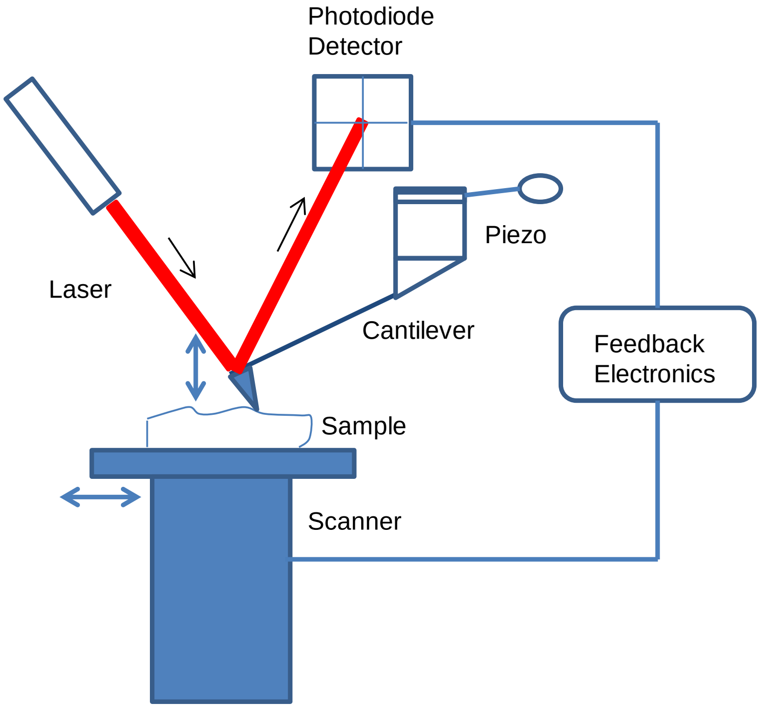

Figure 2.2: Working principles of AFM

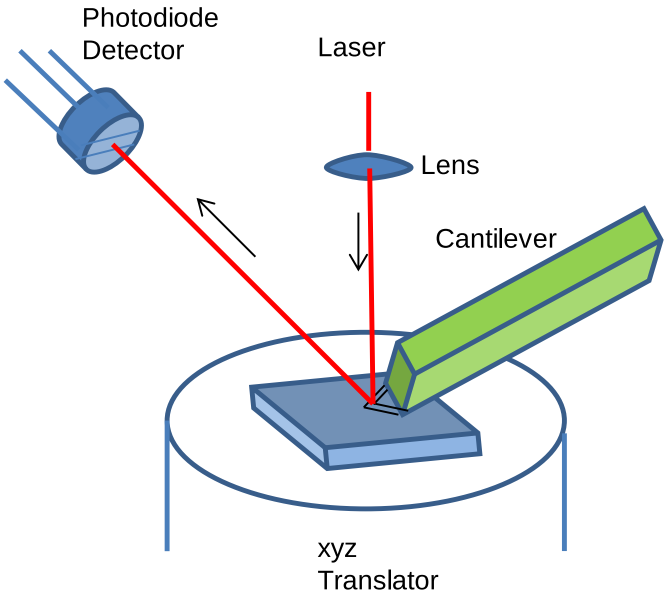

Figure 2.3: Diagram of optical beam deflection

Another way in which measurement errors can happen is if the stylus loses contact with the surface as a result of its speed [21]. Nevertheless, it was found that, for most surfaces, the errors introduced by the stylus speed were minor. Lateral deflection of the stylus has also been considered as a source of error. The effect of lateral deflection on profile measurement was also determined to be inconsequential when compared to the dimensions of the stylus [21].

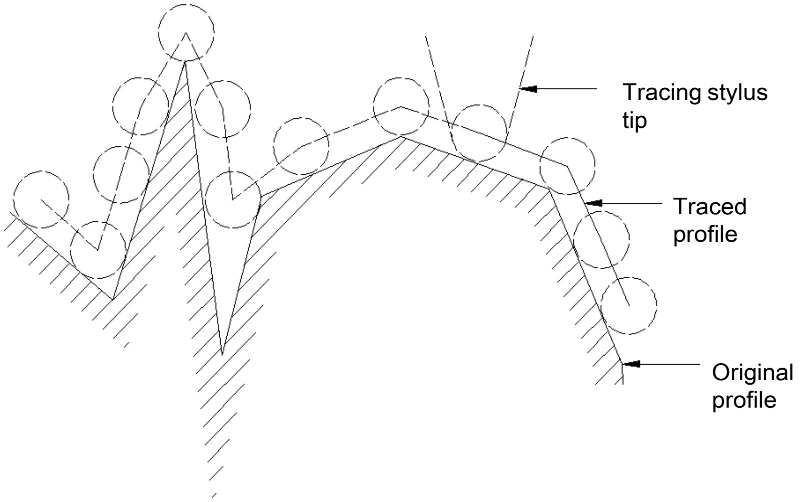

Figure 2.4: Distortion of a surface profile due to the effect of stylus size

2.1.2.2 Optical Instruments

The second technique of measuring surface roughness is using optical instruments.

A beam of electromagnetic radiation can be reflected off a surface in three different ways: specularly, diffusely, or both [21]. This is illustrated in Figure 2.5.

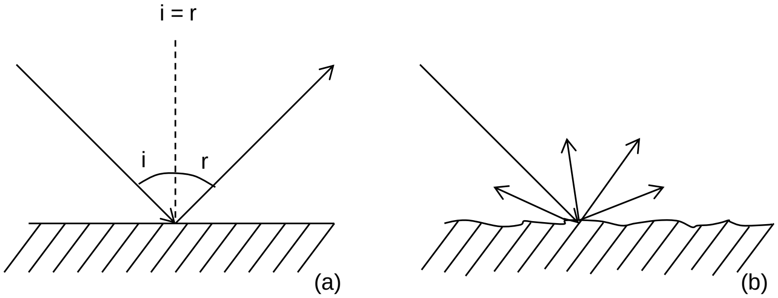

Figure 2.5: Modes of reflection: (a) Specular; (b) Diffuse

Depending on the surface roughness, radiation of a certain wavelength may be reflected specularly, while radiation of another wavelength may be reflected diffusely. Thus, the amount of specular and diffuse reflection can be used to determine surface roughness.

One instrument that employs specular reflection to characterize roughness is the light-section microscope [21]. An image of a slit is projected onto the surface and the objective lens captures the image at the specular reflection angle. If the surface is smooth, the image obtained will be straight; however, if the surface is rough, an undulating pattern will be observed. This instrument is suitable to measure peak-to-valley roughness with a vertical resolution of about 0.5 μm.

The interaction of polarized light with a surface can also be employed to evaluate surface roughness. Such is the case of the long-path length optical profiler, which focuses a laser beam onto a surface by means of an arrangement of mirrors [21]. Before reaching the specimen, the laser goes through a Wollaston prism that polarizes the beam into two orthogonal components. The beams are then focused onto the surface where they reflect back to the prism. Finally, the reflected beams are directed to a beamsplitter, which sends each beam to a different detector. The phase difference of the polarized beams, which is related to the height difference at the surface, results in a voltage difference that can be measured. This instrument was reported to have a vertical range and resolution of 2 μm and 0.025 nm, respectively.

Another instrument that employ optical to measuring surface roughness is Scanning White Light Interferometer which will be used in our study.

2.2 SWLI

2.2.1. Principal of SWLI

SWLI is a versatile technology that provides a noncontact, 3-D method of measuring surface roughness. The interference microscopy technology combines an interferometer and microscope into one instrument.

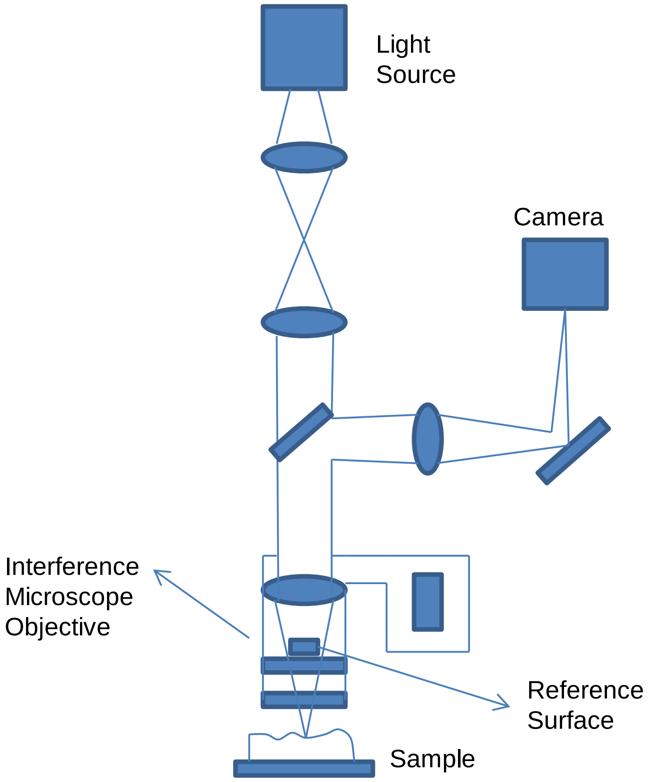

Figure 2.6: Mechanism of SWLI

The mechanism of SWLI is shown in Figure 2.6 [24]. An incoming light beam is split inside the interferometer; one beam is directed to an internal reference surface and the other is directed to the specimen. After reflection, the light beams recombine inside the interferometer, undergoing constructive and destructive interference and producing a pattern of light and dark lines that represents the surface topography of the sample under test. This pattern, known as an interferogram or fringe pattern, is captured by a high resolution CCD camera. A precision vertical scanning transducer then scans the objective in a direction approximately perpendicular to the illuminated surface while a digital camera stores intensity data for each pixel in the field of view. The data acquired in this way consists of an array of interferogram, one for each pixel, representing the variation in intensity as a function of scan positions. Each interferogram is individually processed using frequency domain analysis technique. The final step is the creation of a complete three-dimensional image of the test surface. Lateral measurements are performed by calculating the pixel size from the field of view of the objective in use.

SWLI are capable of measuring a variety of surface types, including ground and polished surfaces, steps and films. By mapping surface heights that range from subnanometers to microns across areas that range from microns to millimeters in a single measurement, SWLI can rapidly provide surface roughness, shape and waviness data.

When the required measurement areas are larger than the field of view, a stitching procedure can be employed that involves a number of partially overlapping measurements being combined into one surface profile. Stitching, however, requires that regions overlap, with the overlapping data aligning adjacent measurements. Because overlap regions are measured more than once, overall measurement time increases [24].

The primary applications for SWLI are surface measurement of MEMS (micro-electromechanical systems) and semiconductors. Other applications include measuring machined material surfaces, micro-fluidic devices, optics and fibers, ceramics, glass, paper, thin films and polymers.

2.2.2. Advantage of SWLI

Unlike conventional coherent interferometric technology, a SWLI uses an incoherent light source. Therefore, its fringe spectrum is wavelength-modulated instead of intensity-modulated, which enables a SWLI to deduce absolute distances from the fringe spectra. This feature is very important for our application as it can handle abrupt height changes that are commonly encountered in the slip band systems of a fatigued surface. In contrast, conventional interferometric microscopes require a continuously varying surface to avoid phase wrapping. Another competing surface profiling instrument is an AFM as mentioned in 2.1.2.1. The imaging area and vertical dynamic range of an AFM, however, are limited. In addition, AFM has a rather slow scan rate because of its point-by-point operation. Compared with an AFM, a SWLI can achieve similar vertical resolution yet possesses several distinguish advantages:

1) Large imaging area: while the maximum imaging area of AFMs is usually 100 μmX100 μm, there is no upper limit on the imaging area of a SWLI since it is essentially an optical microscope and a microscope objective with a lower magnification can be used to accommodate larger imaging area.

2) Easy to change the image range: AFMs usually come with two different image ranges. However, changing the image range requires interrupting the operation to install a designated scanning stage for each specific image range. In comparison, a SWLI can change the image range very easily by switching the microscope objective to a microscope objective with different magnification.

3) Fast scan rate: AFM has the slow scan rate due to its point-by-point operation. A 3D topographic image with a reasonable resolution could take several minutes to acquire (An AFM image of 100 μm^2 takes several minutes). On the other hand, a SWLI can profile a sample area of several square millimeters in a few seconds because the full-view of the sample surface is imaged at once with a CCD camera.

2.2.3. Limitation of SWLI

The principle limitation of SWLI, like any other optical technique, is that it depends on the optical properties of the medium through which it is looking, whether it's glass, air or, for semiconductor manufacturing, thin films. For example, each of the dielectric thin films has its own optical properties, this can produce anomalous results, such as inaccurate film thickness or step measurements, due to the different optical properties of the films. Most instrument manufacturers have proprietary methods of overcoming these anomalies, but the ambiguity remains [25].

Also, SWLI is typically focused on the vertical resolution, or topography, and less on lateral resolution, such as the part's geometric dimensions. Thus, it may lack lateral resolution to capture structure with very small lateral dimensions.

2.2.4. SWLI in Use

The SWLI being used in our study is VEECO Wyko NT9100 Optical Profiler. It has a 0.1 nm vertical resolution and a minimum lateral resolution of 0.20 μm for a 50X objective lens with 1.0X field of view lens. Based on slip band measurements using AFMs [18], it is estimated that the height of the slip bands is usually larger than 100 nm and the spacing between the slip bands is typically larger than 1 μm. Therefore, the SWLI has the resolution needed to capture the microstructure features generated by fatigue process.

2.2.5. Comparison of SWLI & AFM

To better illustrate the differences between SWLI and AFM, the following table is presented.

Table 1.1: Comparison of SWLI and AFM

Features	SWLI	AFM
Image area	Large	Small
Changing image range	Easy	Hard
Scan rate	Fast	Slow
Vertical resolution	Up to 0.1 nm	Up to 0.1 nm
Lateral resolution	200 nm (50X Objective &1.0X FOV Lens)	Around 30 nm
Mode	Non-contact	Contact & non-contact

CHAPTER 3

EXPERIMENT DETAILS

3.1 Fatigue Specimen Design and Preparation

The material being studied in this work is an AISI 316L stainless steel supplied by MSC Industrial Supply Co.. It is a widely used austenitic stainless steel for industrial equipment that prevents the corrosive process. Its chemical composition is given in Table 3.1 [26]. The studied material has an average grain size, determined by the linear intercept method, of approximately 30 μm, see Figure 3.1.

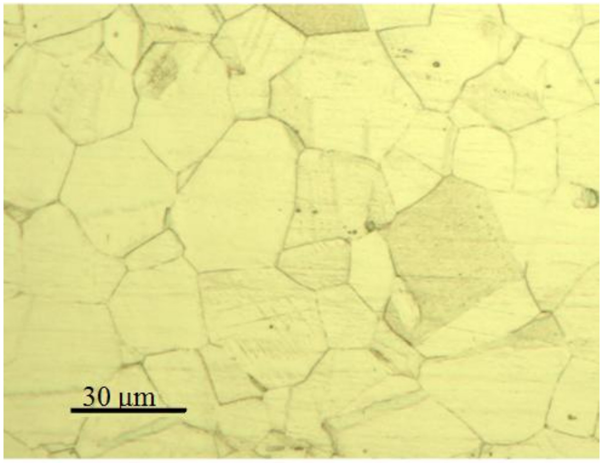

Figure 3.1: Microstructure of AISI 316L stainless steel observed after chemical etching.

Table 3.1: Composition of the AISI 316L stainless steel used in this study (wt.%)

C	Cr	Ni	Mo	Mn	Si	P	S
0.03	17.8	12.95	2.15	2.0	0.75	0.045	0.030

A fatigue specimen as shown in Figure 3.2 was designed according to ASTM standards (E646-96). Its dimension in millimeter is given in Figure 3.3. The specimen was manually polished on silicon carbide polishing films with grit sizes in the order of 220, 400, 600 and 1500 and then polished with the trident and microcloth (Buehler) on a polisher (Buehler Ecomet 3) as the final polishing. In order to reveal grain boundaries, the specimen was chemical etched in a solution composed of 1 volume HCl and 1 volume HNO_3 for 45 s. The time for the chemical etching was carefully controlled so that the grain boundaries are not etched too much. The initial surface roughness parameter R_a at four different regions (Figure 3.2 & Figure 3.3) on the etched specimen i.e. at the center (a), 2 mm off the center (b), 5 mm off the center (c) and 7 mm off the center (d), were measured using SWLI to be around 90 nm.

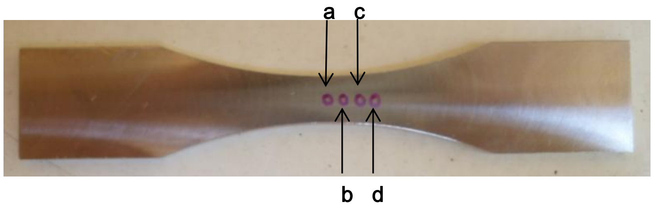

Figure 3.2: Fatigue specimen: surface profiling region

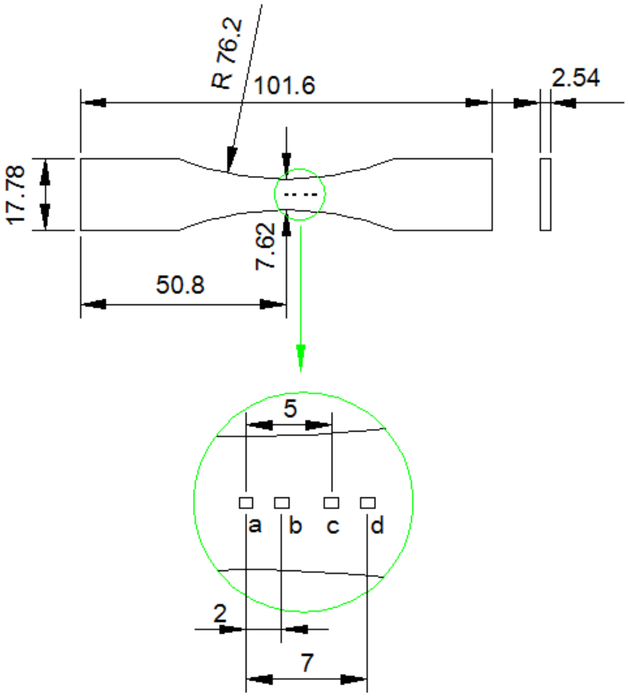

Figure 3.3: Fatigue specimen: specimen drawing (all units in mm).

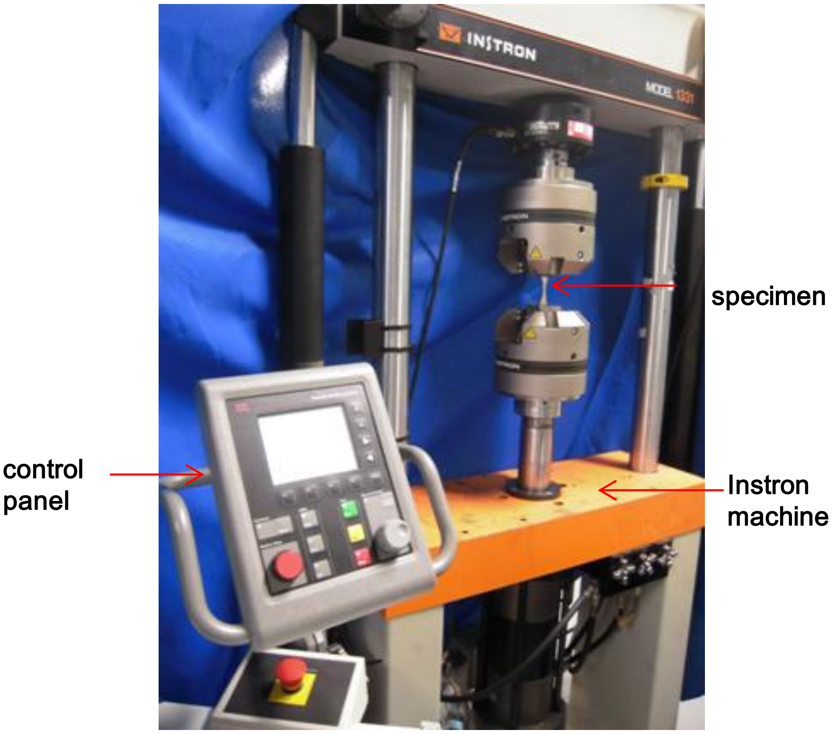

Figure 3.4: Fatigue experimental set-up

3.2 Fatigue Experiment Set-up

In order to study surface roughness evolution of a fatigued specimen, fatigue test was carried out on a servo-hydraulic Instron machine (Figure 3.4). The specimen was subjected to tension-tension fatigue cycling under load control. The maximum load was 2100 lb initially with a load ration of R = 0.5 and a constant loading frequency of 5Hz. During the fatigue process, the maximum load was increased three times, i.e. from 2100 lb to 2200 lb at 1600 cycles, from 2200 lb to 2300 lb at 2800 cycles, and from 2300 lb to 2600 lb at 9400 cycles. In addition, at 5800 cycles, the specimen was overloaded by accident. The specimen eventually fractured at 12500 cycles. The experiment was paused periodically so that the specimen can be removed from the test fixture and inspected under the SWLI.

3.3 SWLI Set-up

A 50X objective and 1X field conversion lens were used to achieve a field of view of approximately $125 \times 93\ \mu m^2$ which was small enough to reveal the fatigue damage at a micro-structural scale. Vertical Scanning Interferometry (VSI) mode which has a vertical range of 10 mm was utilized to capture large surface deformation in this study. The surface topologies at the four regions of the specimen shown in Figure 3.2 were profiled periodically. Typical SWLI measurement results were illustrated in Figure 3.5 and Figure 3.6. Figure 3.5(a) showed the center region of the specimen before fatigue taken by CCD camera of SWLI. Figure 3.5(b) shows the same region profiled by SWLI which gave the surface statistics parameter R_a, R_q, R_z and R_t in the left column. Figure 3.6 illustrated the same region in Figure 3.5 after 200 fatigue cycles.

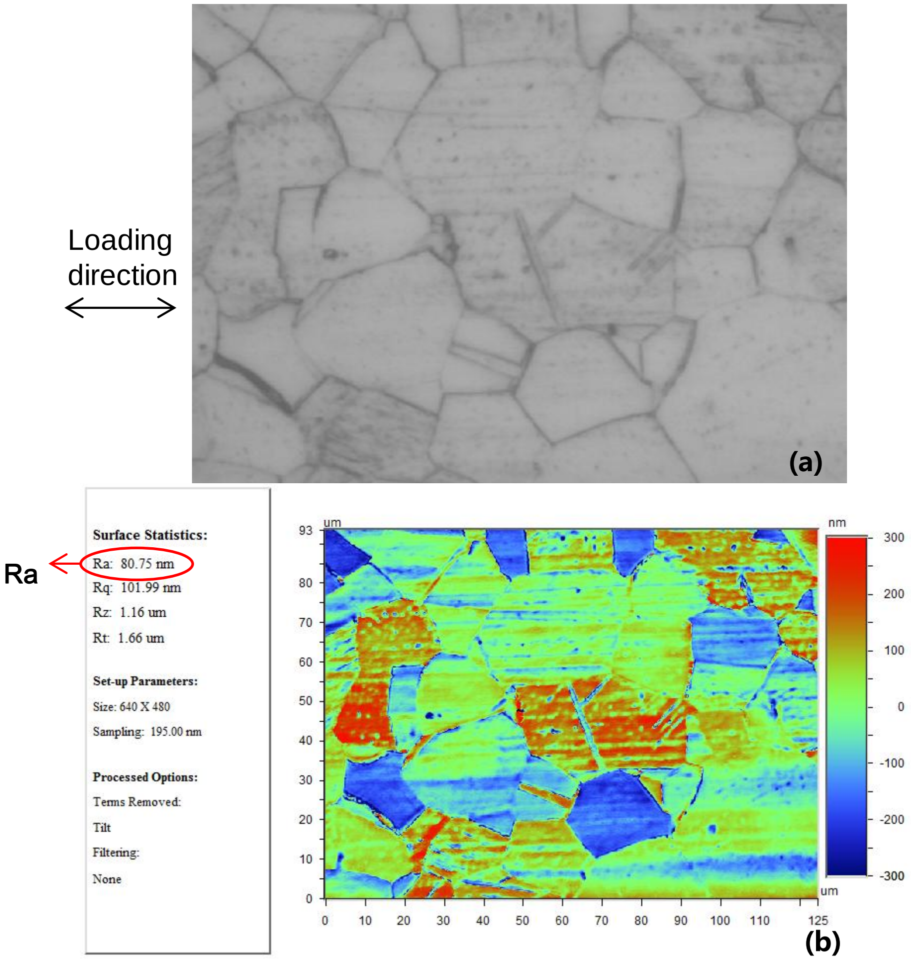

Surface Statistics:
Ra: 80.75 nm
Rq: 101.99 nm
Rz: 1.16 um
Rt: 1.66 um

Set-up Parameters:
Size: 640 X 480
Sampling: 195.00 nm

Processed Options:
Terms Removed:
Tilt
Filtering:
None

Figure 3.5: Surface pattern at the center region before fatigue; (a) taken by CCD camera; (b) profiled by SWLI.

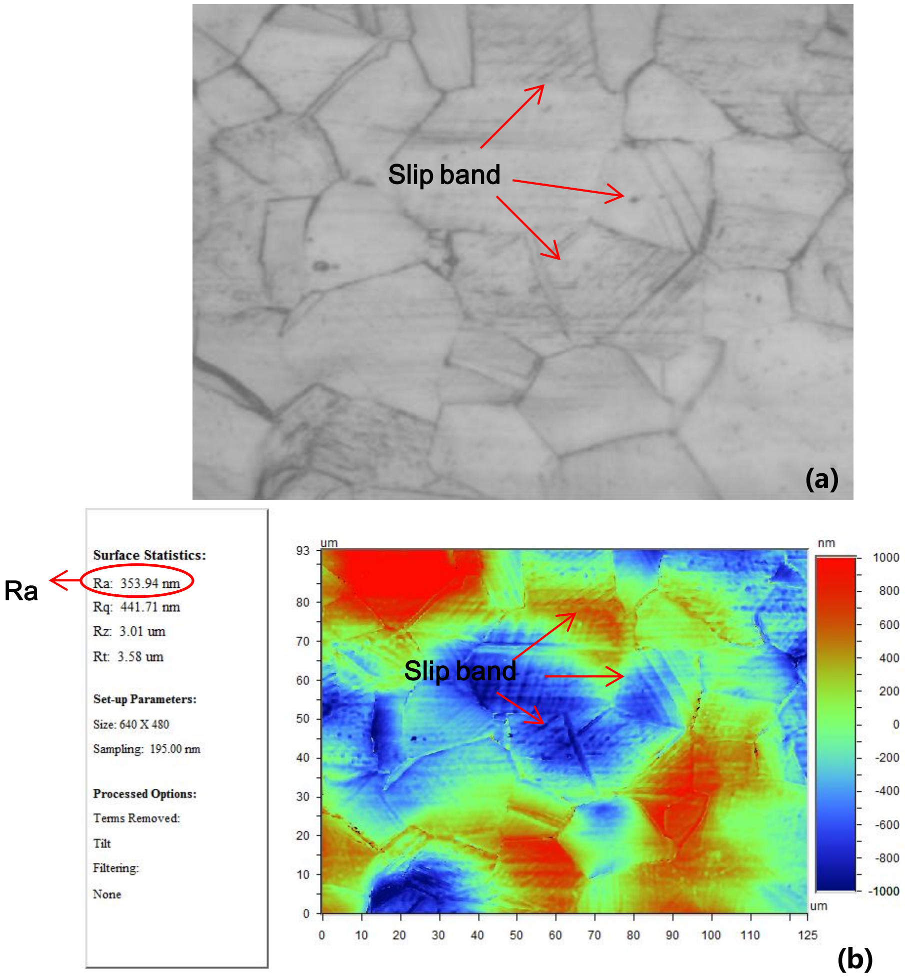

Surface Statistics:

Ra: 353.94 nm

Rq: 441.71 nm

Rz: 3.01 um

Rt: 3.58 um

Set-up Parameters:

Size: 640 X 480

Sampling: 195.00 nm

Processed Options:

Terms Removed:

Tilt

Filtering:

None

Figure 3.6: Surface pattern at the center region after 200 fatigue cycles; (a) taken by CCD camera; (b) profiled by SWLI.

From Figure 3.5 and 3.6, it is denoted that the CCD camera can only give 2-D images, while SWLI can provide informative 3-D images to help us quantitatively characterize the complex surface roughening phenomenon. Comparing the profiling pictures shown in Figure 3.5 and Figure 3.6, we found that the surface roughness R_a in the center area increased drastically from 80.75 nm to 353.94 nm with clearly identifiable slip bands after only 200 cycles. Detailed results and discussion of these surface roughness changes will be covered in Chapter 4.

CHAPTER 4

RESULTS AND DISCUSSION

4.1 Surface Roughness Increase with Fatigue Cycling and Load Increases.

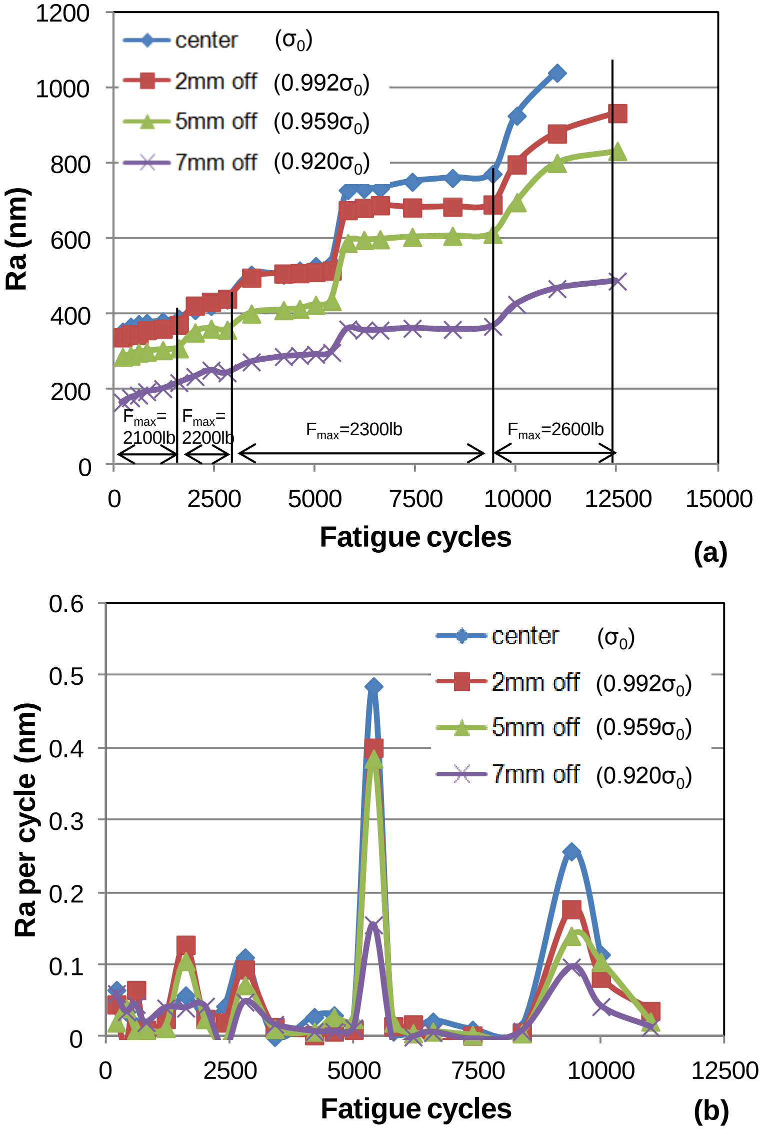

Figure 4.1: Surface roughness increase with fatigue cycling and load increases: (a) R_a increase; (b) R_a increase rate

The surface roughness of the four profiling zones were measured periodically and plotted against the fatigue cycles in Figure 4.1(a). For all the four regions, the surface roughness increased monotonously with the fatigue cycling. For each load increase during the fatigue process, i.e. at 1600, 2800 and 9400 cycles, the surface roughness responded with a sudden jump. The plastic hardening following the overload can also be observed at 5800 cycles from the surface roughness curve. Also, when load was increased again at 9400 cycles, large plastic deformation occurred until fracture at 12500 cycles. The surface roughness increases for the four regions appeared to be the same. However, the center region, which has the highest stress, had a large surface roughness increase for the first 200 cycles. In addition, this region also had large increases during overloading, especially at 5800 cycles. As a result, the surface roughness decreases steadily as the sampling region moved away from the center high stress region. The R_a increase rates were also plotted in Figure 4.1(b) and the four peaks correspond to three load increases and one overload denoted above. To quantitatively see how the stress changes, the stress distribution in those four regions were also simulated by ANSYS. If we set the stress at center region to be σ_0, the stresses in the other three regions are $0.992\sigma_0$, $0.959\sigma_0$ and $0.920\sigma_0$, respectively, as shown in Figure 4.1.

4.2 Underlying Mechanisms.

4.2.1 Slip bands development

To understand the mechanisms that contribute to the surface roughness increase, 3D surface profile images of the specimen were inspected. As shown in Figure 3.6, some grains have fully developed sets of slip bands while the neighboring grains have no slip bands development after 200 cycles. This is reasonable because the development of slip bands in a given grain depends strongly on the orientation of the active slip system within that grain. If no active slip system is oriented towards the surface of the material or if the interaction of the several slip systems creates a three-dimensional arrangement of dislocations (e.g. cellular of labyrinth structure) which prevents the development of large scale slip along a single band, surface upsets cannot form and a smooth grain surface is observed [16]. Figure 4.2 shows the typical evolution of the slip bands within a grain at the region that is 2 mm from the center region. For the 1st 2000 cycles, the height of the slip bands increased steadily with the fatigue cycles. However, the height of the slip bands did not change much from 2000 cycles to 5000 cycles. To quantitatively evaluate the evolution of the slip bands, the surface roughness of the slip bands were calculated along a line that is perpendicular to the slip bands and plotted versus the fatigue cycles in Figure 4.2 (b). It clearly shows that the surface roughness of the slip bands increased linearly with the fatigue cycle for the 1st 2000 cycles while the surface roughness remained constant after 2000 cycles. This indicates that slip band development is the main contributor for the surface roughness increases at low fatigue cycles (<2000 cycles) but there is a different mechanism that contributed to the overall surface roughness increases of the specimen after 2000 fatigue cycles.

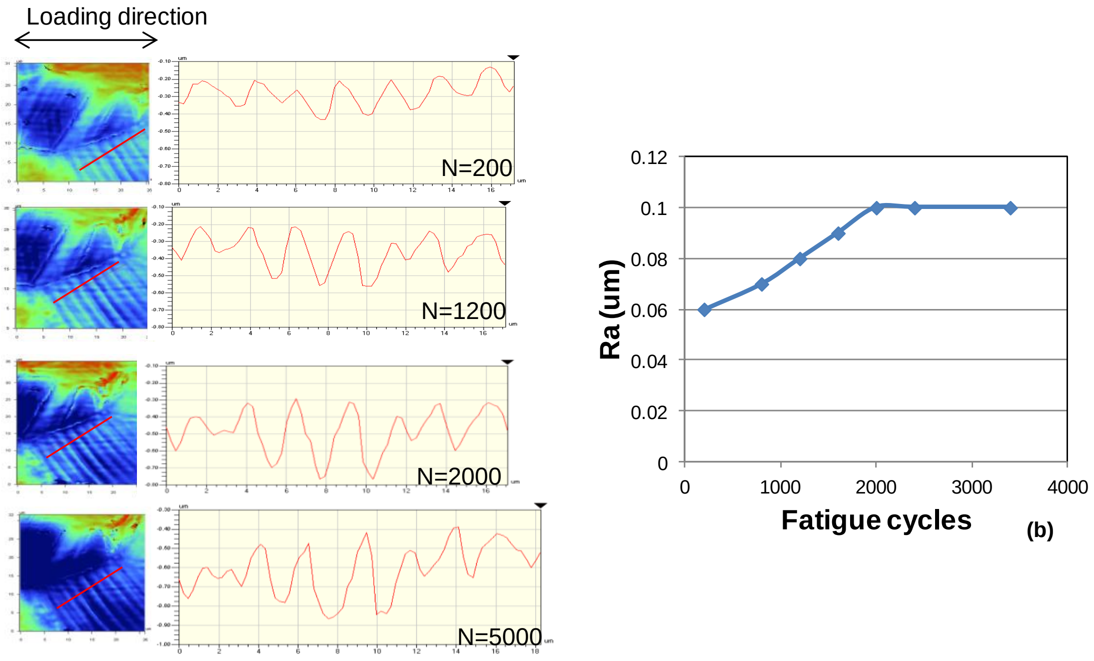

(a) **(b)**

Figure 4.2: Surface profile of slip bands at 2mm off center region; (a) Slip band height at different fatigue cycle; (b) Surface roughness of slip band vs. fatigue cycle.

Evolution of the slip bands at different locations has also been studied. The detected slip bands were all at angles between 30º and 80º with the loading axis. Figure 4.3(a) shows the

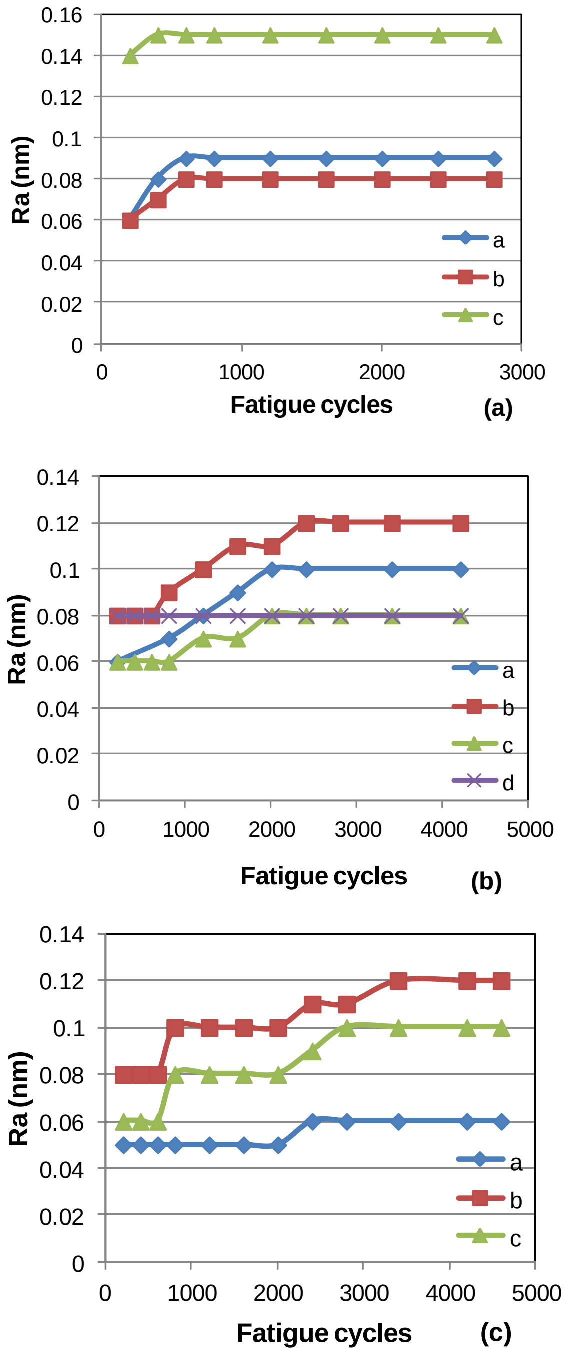

Figure 4.3: Surface profile of slip bands at different locations; (a) Center region; (b) 2 mm off the center region; (c) 5 mm off the center region.

slip bands evolution at three different grains in the center region. The growth of the slip bands saturated before 800 fatigue cycles in this region. The slip bands evolutions at four different grains in the region that is 2 mm from the center were shown in Figure 4.3(b). The average saturated cycles of the slip bands in this region was 2133 cycles, which is more than that of the center region. Similarly, it took more cycles for the slip bands in the region that is 5 mm off the center to saturate than those in the other two regions, as shown in Figure 4.3(c). The saturation cycle of each set of slip bands and the average saturation cycle in each region are tabulated in Table 4.1. The average saturation cycle in Table 4.1 with a 95% confidence level was plotted in Figure 4.4. Table 4.1 and Figure 4.4 clearly indicates that the saturation cycle tends to increase as the sampling region moved away from the center high stress region. Thus, we can conclude

Table 4.1: Saturation cycle of slip band

	Center region	2 mm off the center region	5 mm off the center region
a	400	2000	2400
b	600	2400	3400
c	600	2000	2800
average saturation cycles	533	2133	2867

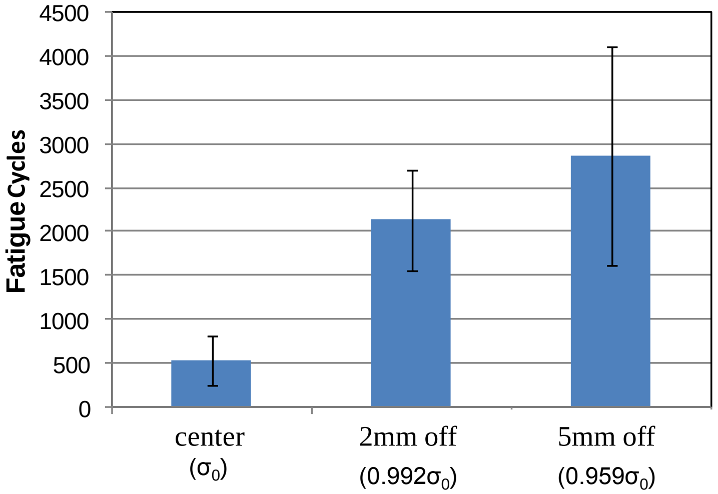

Figure 4.4: Saturation cycle at different sampling region with a 95% confidence level.

that the local stress field plays an important role in the slip band development. We also discovered that the surface roughness along the slip bands at some of the grains (line d in Figure 4.3(b) and line a in Figure 4.3(c)) has little development during the fatigue process. This can also be explained by the orientation of the slip systems in that grain, some of which prevents the development of large scale slip action [16].

4.2.2 Out-of-plane Displacement between Adjacent Grains

Although the height of the slip bands saturated at early fatigue stage, the surface roughness of the sampled regions kept increasing with fatigue cycling. To identify the second mechanism that contributes to the surface roughness increases, we investigated the height difference between adjacent grains.

We found that at initial fatigue cycles, almost all the grains were of the same height. As the fatigue cycle increase, some of the grains gradually moved up while some others “sunk” down. The change of height difference between two adjacent grains is shown in Figure 4.5. The height difference increased slightly for the first 1600 cycles but experienced a large jump when the load was increased from 2100 lb to 2200 lb at 1600 cycles. Immediately after the load increases, the height difference remained almost constant for several hundred cycles but increased again when the maximum load altered from 2200 lb to 2300 lb at 2800 cycles. For the overloading at 5800 cycles, the height difference also responded with a sudden jump. This indicates that stress field again has an impact on the development of the height difference between adjacent grains. A more visual representation of the out-of-plane displacement between the two grains in Figure 4.5 is shown in Figure 4.6.This kind of out-of-plane displacement i.e. grains “pop out” or recede, also occurred between adjacent grains in other sampled regions as shown in Figure 4.7

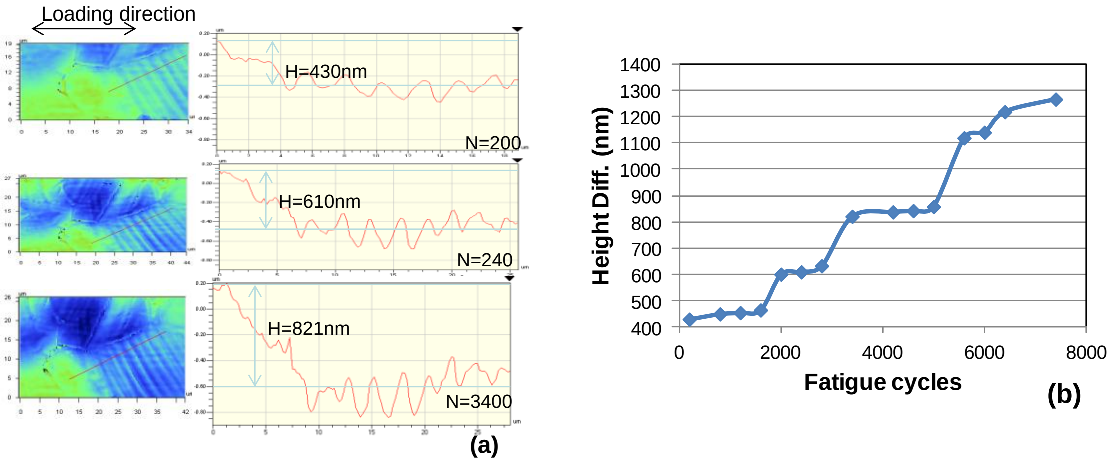

Figure 4.5: Height change between two adjacent grains at 2mm off center region; (a) Surface profile images; (b) Height difference vs. fatigue cycle.

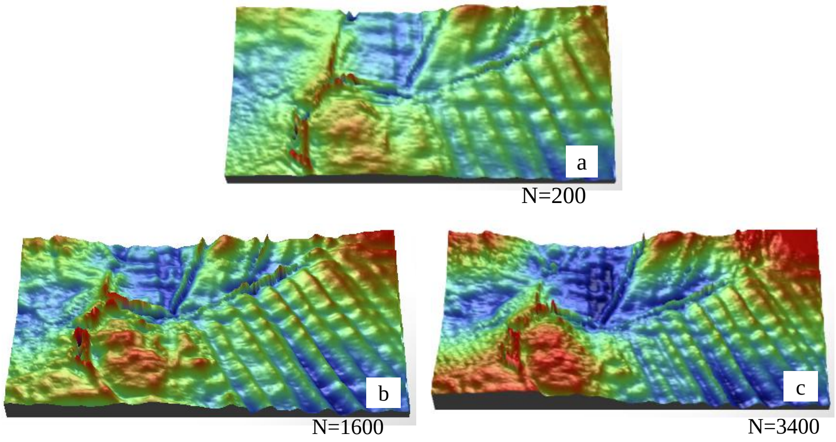

Figure 4.6: 3D pictures on surface relief evolution.

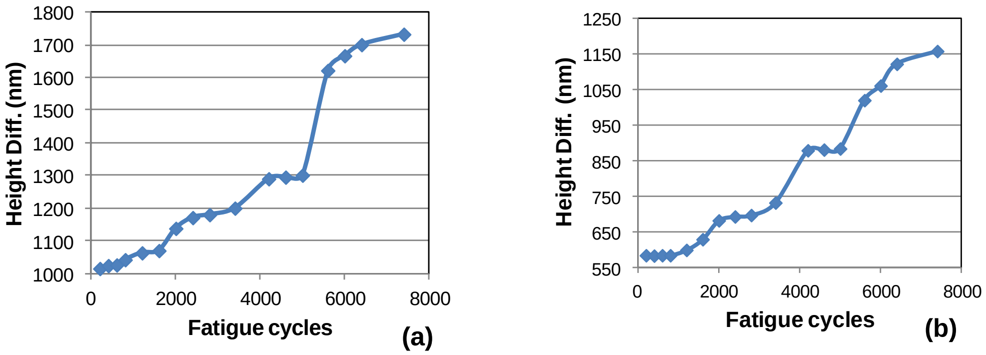

Figure 4.7: Height difference vs. fatigue cycle: (a) Center region; (b) 5 mm off the center region.

4.3 Micro-crack Initiation and Development

Very few micro-cracks were detected at the specimen surface through the whole fatigue progress. The 2D micrographic images and the 3D surface profiling images of micro-cracks initiated at two regions are shown in Figure 4.8(a)&(b) and Figure 4.8(c)&(d), respectively. In Figure 4.8(a), the micro-cracks were initiated at the grain boundary while the micro-cracks in Figure 4.8(b) were initiated inside the grain. We may draw the conclusion that there are two different mechanisms for micro-crack formation based on the observation of these two regions. However, the 3D surface profiling images indicated that the micro-cracks at both regions were initiated at the depth changing region and all of them propagated inside the recessed regions. This is consistent with the stress concentration theory because the depth changing regions have high stresses due to the stress concentration effect. In addition, for the region shown in Figure 4.8(a)&(c), the micro-cracks were confined within the grain boundaries because the grain in front of the micro-crack is higher than the grain contains the micro-crack. For the region shown in Figure 4.8(b)&(d), the micro-cracks actually propagated to the next grain because the grain in front of the micro-cracks is lower than the grain containing the micro-cracks. Figure 4.8 clearly shows that the 3D surface profile images provide much more information about the micro-crack initiation and propagation than the 2D images.

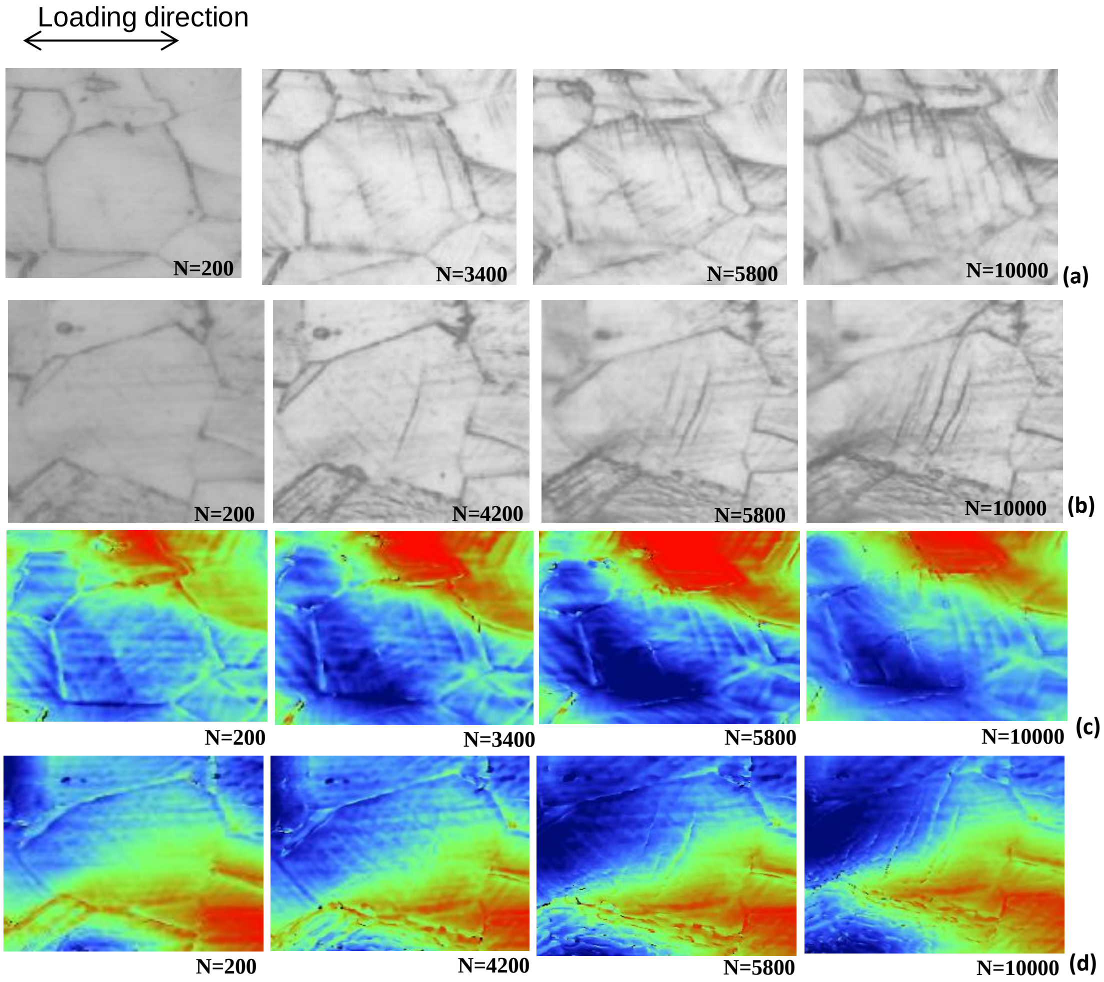

Figure 4.8: Micro-cracks development at two regions; (a) and (b): Two dimensional micrographic images;(c) and (d): Three-dimensional surface profiling images.

CHAPTER 5

IMPROVED FATIGUE EXPERIMENT

5.1 Improved Fatigue Experiment

5.1.1. Fatigue Specimen Redesign

In the previous fatigue experiment, the fatigue specimen was cracked not from exactly the center region that we were monitoring. In order to reveal the relationship between the slip band development and micro-crack initiation and propagation, we decide to redesign the specimen to make sure that the specimen break at the center. Thus, the fatigue specimen was redesigned according to ASTM standards (E646-96). A comparison of the previous and redesigned specimen was shown in Figure 5.1. The curvature of the new specimen was made

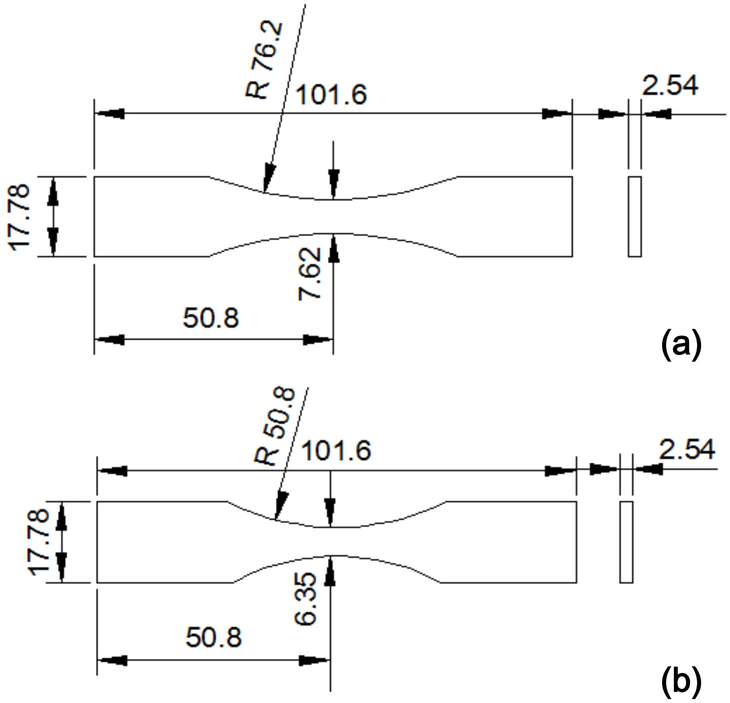

Figure 5.1: Comparison on the previous and redesigned fatigue specimen: (a) Previous specimen; (b) Redesigned specimen.

smaller compared to the previous design. The stress distribution analyzed by ANSYS was illustrated in Figure 5.2. The red region in Figure 5.2 represented the highest stress region which is the most likely site for the specimen to break. The new design provides high stress concentration at the center of the specimen, thus increases the possibility that the specimen will break at the center.

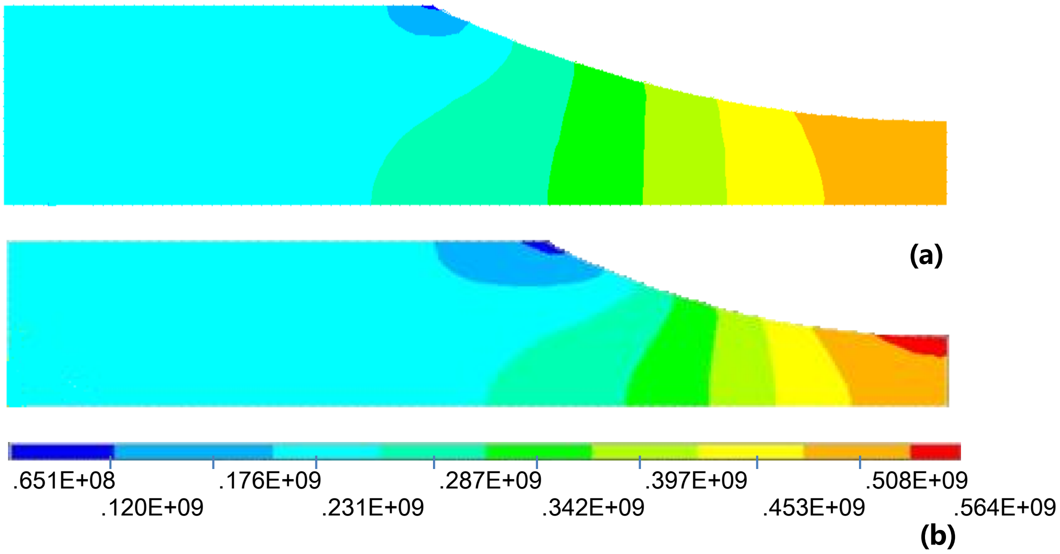

Figure 5.2: Stress distribution in fatigue specimen: (a) Previous specimen; (b) Redesigned specimen.

5.1.2. Heat Treatment

The new fatigue specimen was heated to 800°C for 2 hours after machining. This reduced the residue stress produced during machining which might interfere with the measurement results.

5.1.3. In-situ Camera

In-situ camera was set up before fatigue experiment in order to monitor the surface damage evolution in real time during the fatigue test and to acquire images at the micro-structural scale. The camera consists of a 10-bit charge-coupled device (CCD) camera to observe a zone of 365×260 μm^2. This zone was able to reveal the fatigue damage at several grains in one image. The in-situ observation device was mounted on motorized translation stages that can move the camera perpendicular and parallel to the studied specimen surface (See Figure 5.3).

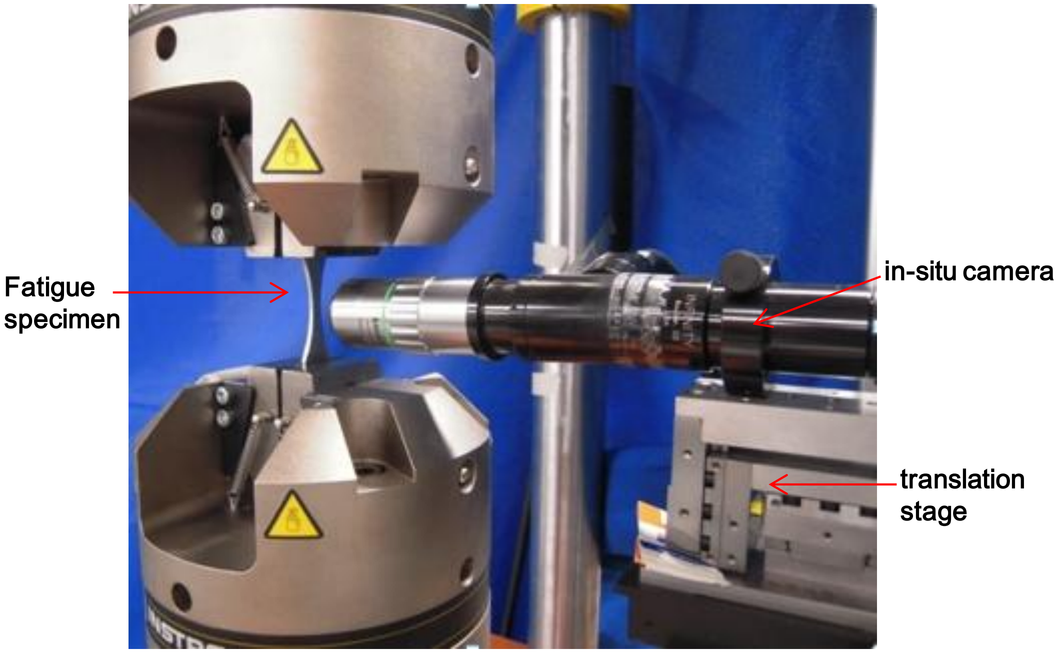

Figure 5.3: In-situ camera set-up.

A domain of 9 consecutive images was observed during the test (Figure 5.4). The total dimensions of the observation domain were 3175 μm × 260 μm. Images of this domain were first acquired before the test. Then, during the test, the machine was stopped every several hundred cycles and 9 consecutive images were taken. Every image of a given zone was taken with a lot of precaution in order to represent exactly the same zone of the specimen, which enables to observe the fatigue damage changes at the specimen surface directly. With the assist of the in-situ measurement, we can easily tell when there is an evident change in the surface feature and decide when to surface profile the specimen in SWLI. The same domain was also observed using the Veeco surface profiler so that the 3D surface profiles can be compared with the in-situ images.

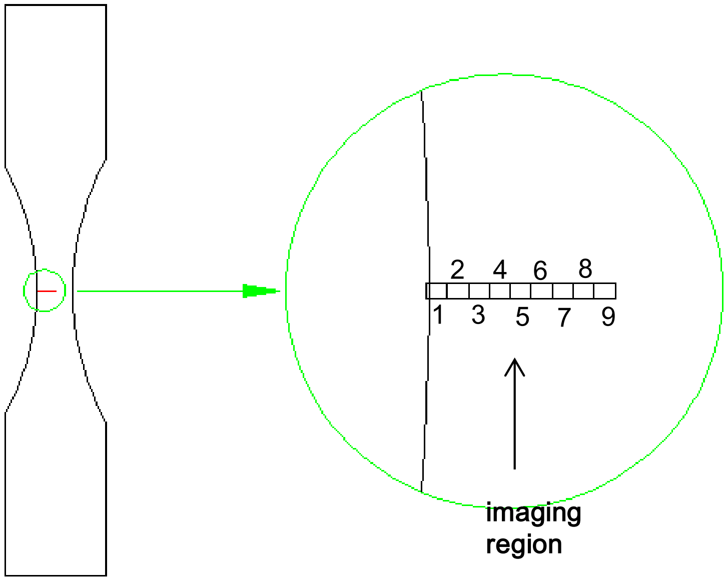

Figure 5.4: Inspection region on the redesigned fatigue specimen.

5.2 Experiment Details

The redesigned fatigue specimen was polished and etched as described in Chapter 3. The specimen was subjected to tension-tension fatigue cycling under load control. The maximum load was 1000 lb initially with a load ration of R=0.5 and a loading frequency 5 Hz. During the fatigue process, the maximum load was increased 7 times, i.e. from 1000 lb to 1200 lb at 40000 cycles, from 1200 lb to 1400 lb at 46000 cycles, from 1400 lb to 1500 lb at 50000 cycles, from 1500 lb to 1600 lb at 52000 cycles, from 1600 lb to 1700 lb at 56000 cycles, from 1700 lb to 1900 lb at 74000 cycles and from 1900 lb to 2100 lb at 80000 cycles. The experiment was stopped at 86000 cycles when the specimen was substantially stretched.

5.3 Results and Discussion

5.3.1. Surface Roughness Increase with Fatigue Cycling and Load Increases.

The surface roughness were measured covering five 125×93 μm^2 profiling regions: two (a and b) located in zone 1 of Figure 5.4, one (c) in zone 2, another one (d) in zone 4 and the last one (e) in zone 9. Profiling regions a and b in zone 1 were demonstrated in Figure 5.5. Similarly the location of region c, d and e were illustrated in Figure 5.6, 5.7 and 5.8.

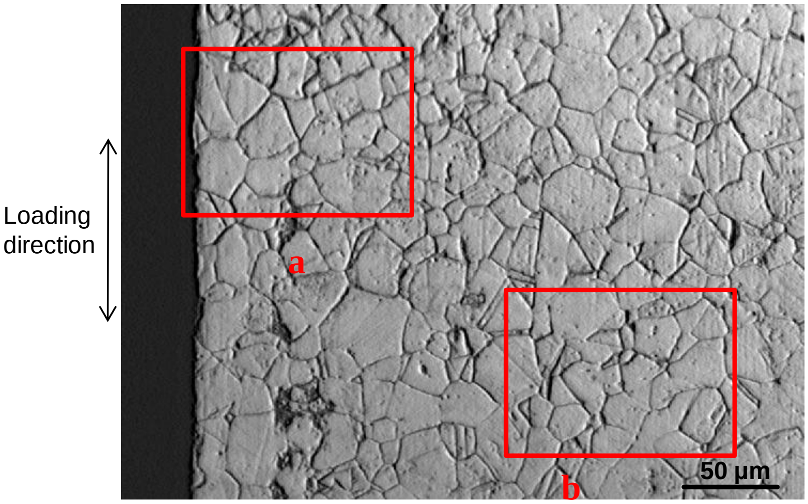

Figure 5.5: SWLI profiling region a and b in in-situ zone 1. (The upper left is region a; The lower right is region b)

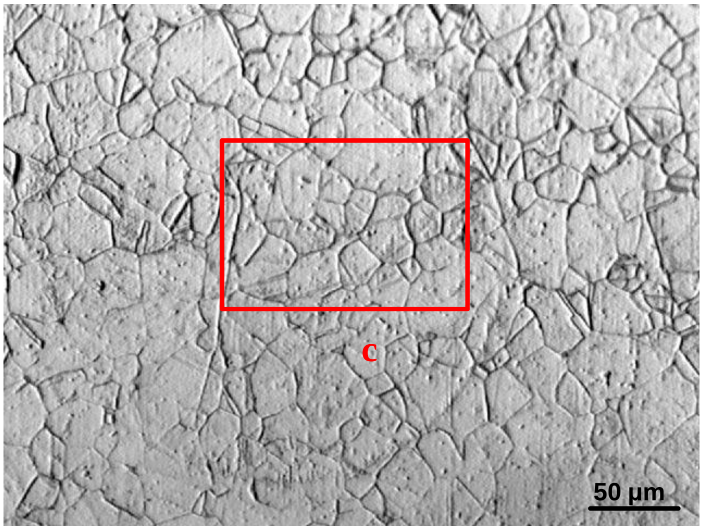

Figure 5.6: SWLI profiling region c in in-situ zone 2.

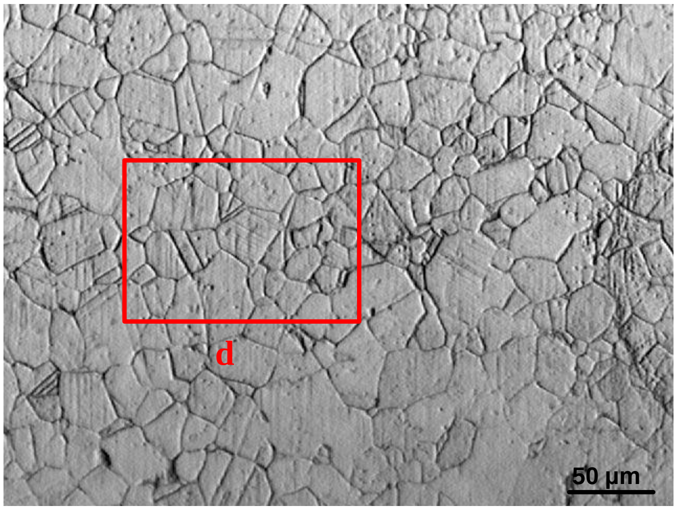

Figure 5.7: SWLI profiling region d in in-situ zone 4.

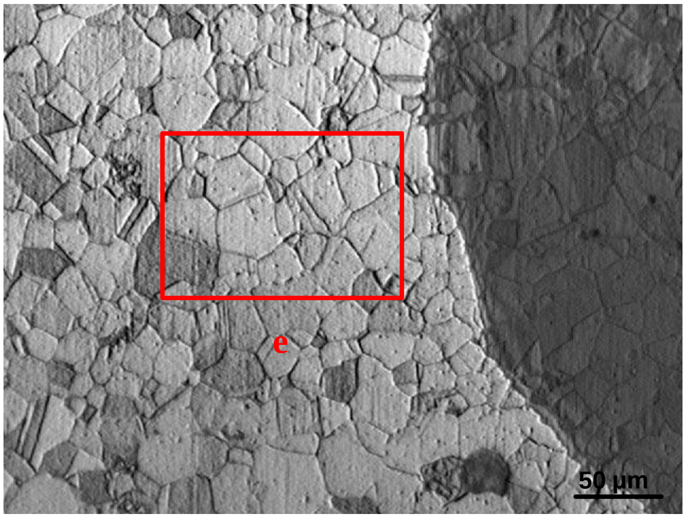

Figure 5.8: SWLI profiling region e in in-situ zone 9.

Figure 5.9(a) shows the surface roughness evolution at those five regions. For each load increase during the fatigue process i.e. at 40000, 46000, 50000, 52000, 56000, 74000 and 80000 cycles, the surface roughness responded with a sudden jump. The stress was the highest in region a (at the edge of the specimen). Therefore, the surface roughness was the highest as well. The surface roughness reduced accordingly as the sampling region moved away from the edge. The reduction was due to the decreasing of the stress level. The R_a increase rate was also plotted in Figure 5.9(b) and the peaks corresponds to load increases during the fatigue. To clearly see how the stress changes, the stress distribution in those five regions were also simulated by ANSYS. If we set the stress at region a to be σ_0, the stresses in the other four regions are $0.996\sigma_0$, $0.979\sigma_0$, $0.939\sigma_0$ and $0.908\sigma_0$, respectively, as shown in Figure 5.9.

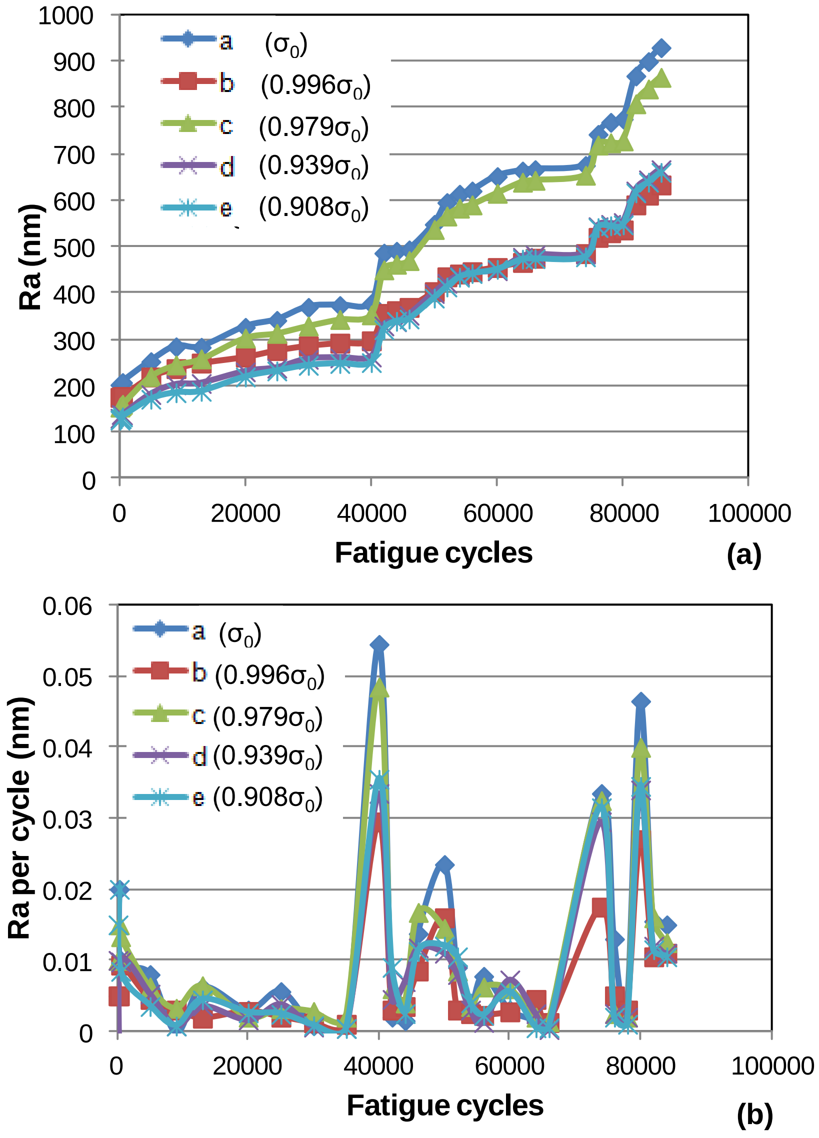

Figure 5.9: Surface roughness increase with fatigue cycling and load increases: (a) R_a increase; (b) R_a increase rate

5.3.2. Slip band development

The slip bands displayed similar behavior as those discussed in the previous fatigue experiment, i.e. initiated at few hundred cycles, grew, fully developed and saturated. The surface roughness evolution of one typical slip in each surface profiling area was plotted in Figure 5.10 respectively. It again indicates that the saturation cycle tended to increase as the stress decreases. It is noteworthy that the average saturation cycles in the new experiment was higher than the previous one due to the lower of the initial fatigue load.

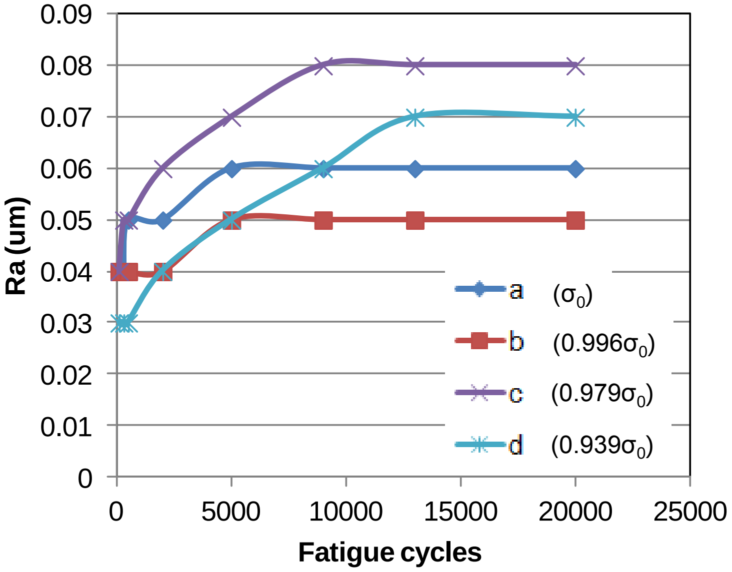

Figure 5.10: Surface profile of slip bands at different locations.

5.3.3. Out-of-plane Displacement between Adjacent Grains

Surprisingly, the area surface roughness in region b was lower than that of region c which has smaller stress than region b, as presented in Figure 5.9 after 5000 cycles. Based on our pervious observation of out-of-plane grain displacement contributing to the later-stage surface roughness increase, the displacement between adjacent grains should be studied again. Three sets of height differences between adjacent grains (grain 1 to grain 2, grain 3 to grain 4 and grain 5 to grain 6) were studied in surface profiling region b and c, as shown in Figure 5.11. These grains had the same heights before etching. The height differences between adjacent grains were measured at different cycles, i.e. 100, 9000, 30000, 42000, 53000, 76000 and 80000. The evolution of average height differences in each region was plotted in Figure 5.12. It was clearly showed in Figure 5.12 that at the beginning, the average height differences between those two regions were not distinctly different. As the fatigue cycles went on, the average height differences in region c increased faster than region b which was coincident with the increase rate of area surface roughness. Thus, it can be concluded that the out-of-plane displacement of adjacent grains was the main contributor to the surface roughness increase in the late fatigue stage.

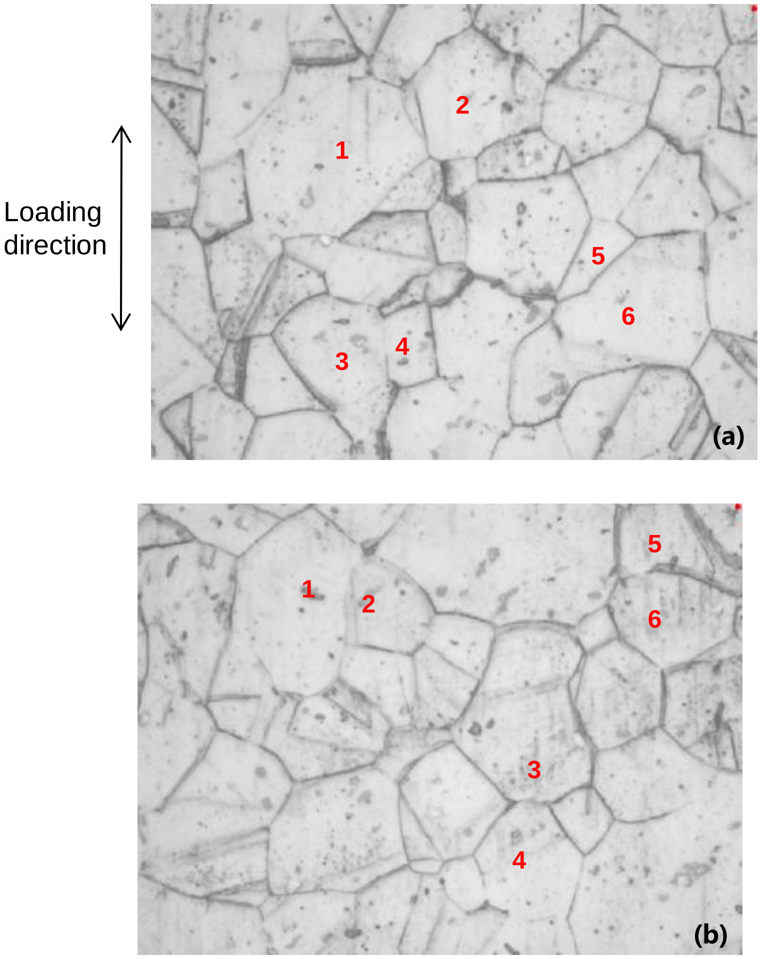

Figure 5.11: The studied adjacent grains: (a) region b; (b) region c.

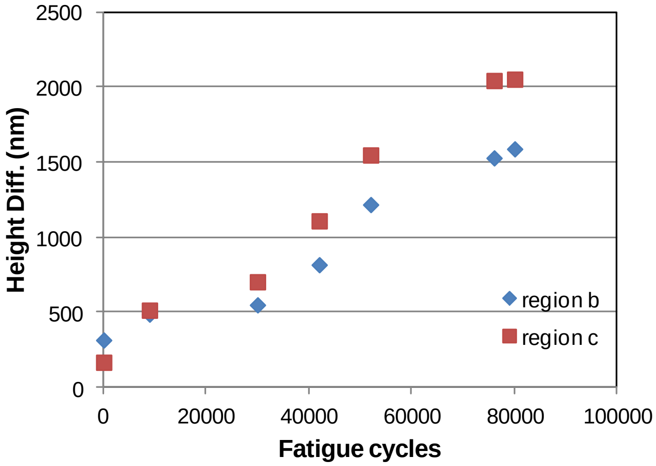

Figure 5.12: Average height change between two adjacent grains in region b and region c.

5.3.4. Micro-crack Initiation

Micro-crack was investigated during the entire fatigue progress, but few were found.

One micro-crack was initiated at grain boundary at 42000 fatigue cycles in region 3. The 2D micrographic image and the 3D surface profiling image of micro-cracks were shown in Figure 5.13. The 3D surface profiling images indicated that the micro-crack was initiated at the depth changing region. This was consistent with what we find in the previous fatigue experiment (the depth changing regions is the most possible region for a micro-crack to initiate due to the stress concentration effect).

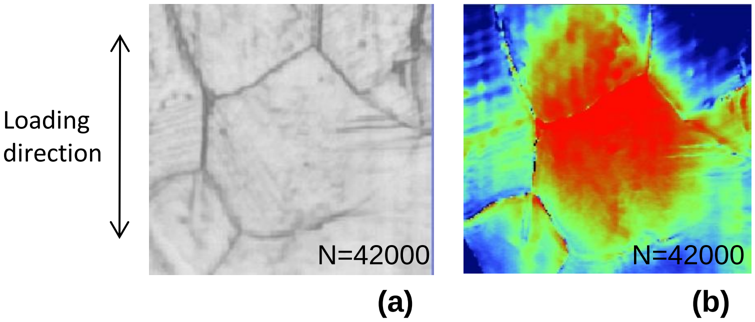

Figure 5.13: Micro-crack development at region c: (a) Two dimensional micrographic images; (b) Three-dimensional surface profiling images.

5.3.5. Possible reasons for lack of Micro-cracks

We only found a few micro-crack initiations in both fatigue experiments. The possible reason for in-situ camera unable to locate the micro-crack is the contrast. One picture taken by in-situ camera on an unetched redesigned fatigue specimen (same as in Figure 5.1b) after 200 fatigue cycles with maximum load 1600 lb, load ration of R=0.5 and a loading frequency 5 Hz was shown in Figure 5.14. The red region was the mark left by the mark pen. Figure 5.14 illustrates that no distinct micro-crack can be detected from the left side of the picture, while micro-cracks are obvious in the marked area.

Figure 5.14: Micro-cracks development at marked area.

Contrast problem should also exist in SWLI, and moreover, the micro-cracks were sealed when there was no outer force exerting on the specimen. These result in only a few distinct micro-cracks found in SWLI. it's worth noting that, during these two experiments, the applied load altered several times, resulting in strain hardening of the studied material and turning it into a totally different material which may have better resistance to fatigue. Lastly, the surface of our specimen was well polished and if there were inner defects in the material, the micro-cracks would prefer to initiate in the interior of the material. In order to observe more micro-crack initiations and discover the relation between the evolution of surface relief and crack nucleation, it is necessary to perform in-situ 3D surface profiling of specimens under static and cyclic loading.

CHAPTER 6

CONCLUSIONS

We have shown strong evidences that surface roughness changes is a good indicator of fatigue damage accumulation in the material. The surface roughness of the specimen kept increasing during the entire fatigue stage. We discovered that early fatigue damage is manifested as slip band formation while later-stage fatigue damage is related to the out-of-plane displacement of the adjacent grains. All of the micro-cracks were found in the depth-changing regions, which agree with the stress concentration theory. In order to establish the relationship between the evolution of the surface relief and crack nucleation, performing in-situ 3D surface profiling of the specimens under static and cyclic loading is needed. Further experiment and simulation study are also needed to understand the effect of surface roughness changes on local stress states at the micro- or meso-scale.

REFERENCES

[1] Suresh, S., Fatigue of Materials. 2nd ed. 1998: Cambridge University Press.

[2] Ewing, J.A. and J.C.W. Humfrey, The fracture of metals under repeated alternations of stress. Metallographist, 1903

[3] Forsyth, P.J.E., Exudation of material from slip bands at the surface of fatigued crystals of an aluminium-copper alloy. Nature, 1953. 171: p. 172-173.

[4] Mughrabi, H., F. Ackermann, and K. Herz, Persistent slipbands in fatigued face-centered and body-centered cubic metals. ASTM Special Technical Publication, 1979(675): p. 69-105.

[5] Mecke, K., C. Blochwitz, and U. Kremling, The development of the dislocation structures during the fatigue process of FCC single crystals. Crystal Research and Technology, 1982. 17(12): p. 1557-70.

[6] Jin, N.Y., Formation of dislocation structures during cyclic deformation of F.C.C. crystals. I. Formation of PSBs in crystals oriented for single-slip. Acta Metallurgica, 1989. 37(7): p. 2055-2066.

[7] Holzwarth, U. and U. Essmann, The evolution of persistent slip bands in copper single crystals. Applied Physics A (Solids and Surfaces), 1993. A57(2): p. 131-41.

[8] Mu, P. and Aubin, V., Microcrack initiation in low-cycle fatigue of an austenitic stainless steel. Procedia Engineering, 2010(2): p. 1951-1960.

[9] Buque, C., et al., Dislocation structures in cyclically deformed nickel polycrystals. Materials Science and Engineering A, 2001. 300(1-2): p. 254-262.

[10] Boyd-Lee, A.D., Fatigue crack growth resistant microstructures in polycrystalline Ni-base superalloys for aeroengines. International Journal of Fatigue, 1999. 21(4): p. 393-405.

[11] Kim, W.H. and C. Laird, Crack nucleation and stage I propagation in high strain fatigue--II. mechanism. Acta Metallurgica, 1978. 26(5): p. 789-799.

[12] Differt, K., U. Essmann, and H. Mughrabi, Model of extrusions and intrusions in fatigued metals: II. surface roughening by random irreversible slip. Philosophical Magazine A: Physics of Condensed Matter, Defects and Mechanical Properties, 1986. 54(2): p. 237-258.

[13] Yang, F. and A. Saxena, Mechanisms of fatigue crack initiation in annealed, quenched and tempered 4340 steel. Proceedings of the Institution of Mechanical Engineers, Part C: Journal of Mechanical Engineering Science, 2000. 214(9): p. 1151-1161.

[14] Harvey, S.E., Marsh, P.G. and Gerberich, W.W., Atomic force microscopy and modeling of fatigue crack initiation in metals. Acta Metallurgica, 1994. 42(10): p. 3493-3502.

[15] Nakai, Y., Ohnishi, K. and Kusukawa, T., Observations of fatigue slip bands and stage I crack-initiation process in α-brass by scanning atomic-force microscopy, Small Fatigue Cracks: Mechanics. Mechanisms and Applications, Ravichandran, K.S., Ritchie, R.O. and Murakami, Y., eds. Elsevier Science, Oxford, 1999. p: 343-52.

[16] Villechaise, P., et al., On slip band features and crack initiation in fatigued 316L austenitic stainless steel: Part 1: Analysis by electron back-scattered diffraction and atomic force microscopy, Materials Science and Engineering, 2002. A323: p.377–385

[17] Cretegny, L. and A. Saxena, AFM characterization of the evolution of surface deformation during fatigue in polycrystalline copper. Acta Materialia, 2001. 49(18): p. 3755-3765.

[18] Polak, J., et al., AFM evidence of surface relief formation and models of fatigue crack nucleation, International Journal of Fatigue, 2003. 25: p. 1027–1036.

[19] Essmann, U., U. Goesele, and H. Mughrabi, Model of extrusions and intrusions in fatigue metals- 1. point-defect production and the growth of extrusions. Philosophical Magazine A: Physics of Condensed Matter, Defects and Mechanical Properties, 1981. 44(2): p. 405-426.

[20] Mughrabi, H., The cyclic hardening and saturation behaviour of copper single crystals, Materials Science and Engineering, 1978. 33(2): p. 207-223.

[21] Thomas, T.R., Rough Surfaces. 2nd ed.1999: Imperial College Press.

[22] Bai, C., Scanning Tunneling Microscopy and Its Applications, 2nd ed. 1999: Shanghai Scientific & Technical Publishers.

[23] Ros-Yáñez, T., Houbaert, Y., and Mertens, A., Characterization of TRIP-assisted multiphase steel surface topography by atomic force microscopy, Materials Characterization, 2001, 47: p. 93-104.

[24] O'Mahony, C., Characterization of micromechanical structures using white-light interferometry, Measurement Science & Technology, 2003, 14(10): p. 1807-14.

[25] Woods, S., Understanding scanning white light interferometry, Micro Manufacturing, 2009, 2.

[26] MSC Industrial Supply Co. website: http://www1.mscdirect.com/cgi/NNSRIT2?PMAKA=83079244&PMPXNO=8251962&cm_re=ItemDetail-_-ResultListing-_-SearchResults

BIOGRAPHICAL INFORMATION

Ye Wang was born in Zhengzhou, China in 1986. He earned his Bachelor of Engineering in Materials Processing and Control Engineering from Huazhong University of Science and Technology, China, in June 2009. He came to United States of America for his graduate studies at the University of Texas at Arlington in August 2009. He has been conducting research at the Advanced Sensor Technology Laboratory since Sep 2009. He has two years working experience on Structural Health Monitoring. He published 1 journal paper in optical fiber sensor based corrosion monitoring and passed Fundamentals of Engineering Exam in October 2011. He was awarded Master of Science in Mechanical Engineering from University of Texas at Arlington in May 2012.